The CpFM, an in-vacuum Cherenkov beam monitor for UA9 at SPS

Published by IOP Publishing for Sissa Medialab
Received: *September 27, 2016*
Revised: *January 31, 2017*
Accepted: *March 27, 2017*
Published: *April 28, 2017*

The CpFM, an in-vacuum Cherenkov beam monitor for UA9 at SPS

V. Puill,[a,1] **F. Addesa,**[c] **L. Burmistrov,**[a] **D. Breton,**[a] **V. Chaumat,**[a] **G. Cavoto,**[c] **S. Conforti Di Lorenzo,**[a] **S. Dubos,**[a] **Yu.A. Gavrikov,**[e] **F. Iacoangeli,**[c] **J. Jeglot,**[a] **J. Maalmi,**[a] **A. Natochii,**[d] **R. Rossi,**[b,c] **S. Montesano,**[b] **W. Scandale,**[b,a] **A. Stocchi**[a] **and J.-F. Vagnucci**[a]

[a] *Laboratoire de l'Accélérateur Linéaire (LAL), Université Paris-Sud 11, Centre Scientifique d'Orsay, B.P. 34, Orsay Cedex, F-91898 France*
[b] *CERN, European Organization for Nuclear Research, Geneva 23, CH-1211 Switzerland*
[c] *INFN — Istituto Nazionale di Fisica Nucleare — Sezione di Roma I, Piazzale A. Moro 2, Roma, Italy*
[d] *Taras Shevchenko National University of Kyiv, 60 Volodymyrska Street, City of Kyiv, 01033 Ukraine*
[e] *Petersburg Nuclear Physics Institute, Gatchina, Leningrad Region, 188300 Russia*

E-mail: puill@lal.in2p3.fr

Abstract: The use of bent crystals for beam manipulation in particle accelerators is a well-assessed concept rapidly evolving into practical application. The experiments of the UA9 collaboration at the CERN-SPS have played a key role for a quantitative understanding of channeling and volume reflection mechanisms.

Investigation of the channeling process close to a circulating beam ideally requires in vacuum detectors resolving the single particle, which should be located inside the vacuum pipe itself. Cherenkov radiators are potential candidates for such functionality due the reduced electro-magnetic interaction of the radiator material with the circulating charges and their compatibility with vacuum requirements in the beam pipe.

For this purpose, we developed a device called Cherenkov detector for proton Flux Measurement (CpFM) that aims at counting the number of deflected protons of the beam halo surrounding the circulating beam with an accuracy of 15%.

After a detailed description of the detection chain and its simulation, we present results of beam tests of different configurations, the calibration of the final device and the results of its first operation in the SPS.

Keywords: Beam-line instrumentation (beam position and profile monitors; beam-intensity monitors; bunch length monitors); Cherenkov detectors; Vacuum-based detectors; Photon detectors for UV, visible and IR photons (vacuum) (photomultipliers, HPDs, others)

[1] Corresponding author.

doi:10.1088/1748-0221/12/04/P04029

Contents

2017 JINST 12 P04029

1 Introduction, the UA9 experiment

Charged particles interacting with a bent crystal can be trapped in channeling states and deflected by the atomic planes of the crystal lattice. The use of bent crystals for beam manipulation in particle accelerators [1] is a well-assessed concept rapidly evolving into practical applications. A large number of experimental findings have contributed, in the last three decades, in clarifying our knowledge and in improving our control of crystal-particle interactions. In particular, the experiments of the UA9 collaboration at the CERN-SPS have played a key role for a quantitative understanding of channeling and volume reflection mechanisms [2]. The efficiency of the latter mechanism has been found to be intrinsically very large, whilst the channeling efficiency has been improved by the increased technological expertise in crystal cutting and bending.

The next step is to assess the possibility to routinely use bent crystals in high-energy high-current particle accelerators. Two specific applications are well identified. Crystals may work as

"smart" primary elements in beam halo collimation systems [3] thereby contributing to localize the losses in safe areas of the accelerator circumference. They may also be used as primary deflectors to extract halo particles for an external use, for instance in hadron colliders without perturbing the high-luminosity operation [4].

Figure 1 represents the conceptual sketch of the UA9 experiment. A Silicon bent crystal inserted in the halo give an angular kick of approximately 150 μrad to the protons, according to its bending angle.

A standard multi-stage collimation system [5] is composed by several collimators with a well-defined hierarchy. Primary collimators are the closest elements to the beam and they have to intercept the primary halo particles without interfering with the motion of the core particles. Protons scattered by the primary collimators (RMS deflection angle: 3.4 μrad at 7 TeV for a 600 mm long Carbon Fiber Composite collimator) form the secondary halo and must be intercepted before they are lost in the machine. For this reason secondary collimators, at larger distance from the beam core, are installed downstream of the primaries. The tertiary halo, populated by protons outgoing from the secondary collimators, can be lost in the machine, therefore further absorbers and protection elements are implemented in the most sensitive regions of the machine [6]. On the contrary, the crystal is deflecting 65% [7] of the impinging particles at a large angle at the first turn, with a low probability to create any "single diffractive" events, since it is only few mm long. Circulating halo particles will be extracted in a subsequent turn, reaching a total extraction efficiency of about 80%. All these extracted particles will be concentrated in a "secondary beam" ("deflected halo beam", "extracted beam" or "channeled beam") that will be the one impacting on the counter (figure 2).

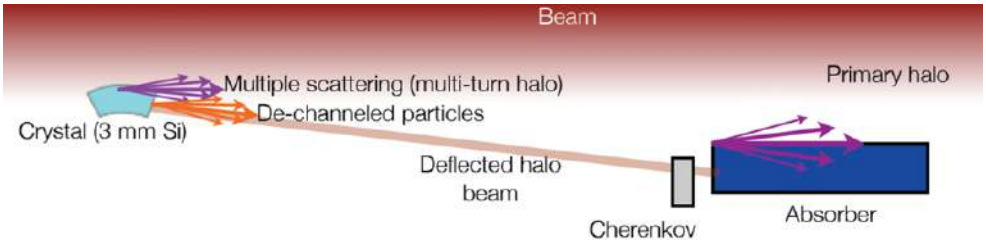

Figure 1. Conceptual sketch of the UA9 experiment.

An optimal characterization of the crystal collimation prototype system requires a novel beam instrumentation to detect and resolve high flux of particles and to eventually identify the debris resulting from the interaction of the incoming particles with the crystal itself. Investigation of the channeling process close to a circulating beam ideally requires detectors which should be located inside the vacuum pipe itself. In its early tests UA9 was able to produce images of the channelling deflected beam during SPS dedicated coast fill [7]. Nevertheless the number of deflected particle (with a population of few hundreds of protons) was never determined in an absolute way.

Beam intensity in a circular accelerator can be measured either with a Beam Current Transformer (BCT), either with a Secondary Emission Monitors (SEM) [8]. In the SPS, BCT are effective for intensities larger than 10^9 particle with a resolution of 5% [9], as to SEM, they are partly destructive (since placed in the beam) and also used for high energy beams ($> 10^6$ particles). Roman Pot can be used to host detectors sensitive to low intensity but there are two inconvenient to the use

of this device: the secondary particles which are created by interaction of protons inside its window can be count as impinging protons and its impact on the machine impedance is not negligible.

Therefore, UA9 started an R&D program in 2012 with the aim of building a proton flux monitor for low intensities and with a precision of 15% or better, to be hosted directly into the beam pipe vacuum.

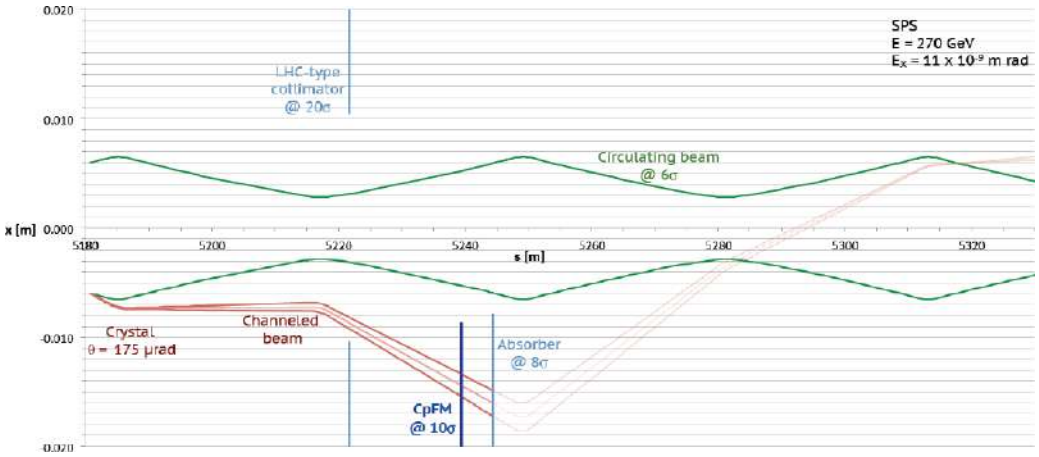

Figure 2. Beam tracking and aperture limitation of the machine in the region of the UA9 experiment in SPS [10]. Primary proton beam (green) and secondary beam (red) envelopes as a function of distance along the ideal trajectory are shown. The position for the installation of the deflected proton counter (CpFM) is shown in blue.

2 Requirements for the proton counter for the CERN accelerators

The counting of the number of deflected protons can be performed by measuring the charge induced by the protons in a particle detector (semi-conductor, gaseous detector), or by measuring the induced light in a radiator that is then detected by a photodetector. The requirements for this device in the SPS environment are listed below:

Vacuum: the detector will be placed inside the primary vacuum (10^{-9} mbar) of the accelerator beam pipe. All its components have to be compatible with the surface cleanliness levels defined by CERN [11].

Impedance: the device should be compatible with the machine parameters.

Timing: the SPS revolution frequency is 43.23 kHz, while for the LHC it is 11.24 kHz. During the operations of the UA9 Experiment one or more bunches are injected into the SPS, accelerated to 270 GeV/c and kept at a constant energy during the experimental measurements. The minimal distance between consecutive bunches is 25 ns (the same as for the LHC standard operations) and the typical bunch length at top energy is close to 2 ns (1 ns in LHC). The detector response has to be fast enough to measure the deflected protons during the duration of one bunch, but it is not required to perform this measurement for each bunch.

2017 JINST 12 P04029

Dynamic range: the counter has to be placed in the shadow of the crystal just in front of the absorber, at a slightly large aperture (7.5 σ from the center of the beam). In the SPS the total intensity of each bunch is around 10^{11} and the crystal extracts around 10^7 particles per second. Depending on the crystal position, the number of protons in the deflected halo will be between few units to 200/bunch which corresponds to the dynamic range of the detector.

Radiation hardness: when placed in operational position, in interaction with the beam halo, the counter will have to stand very high dose (tens of kGy/year). In parking position, the device will constantly live in the SPS radiation field, characterized by the shower particles (photons, pions, neutrons, protons, ...) generated by beam losses at the aperture restrictions of the accelerator (neutron flux of around 10^{12}/cm^{2}and integrated dose of several tens of Gray per year in the immediate vicinity of the beam pipe).

Occupancy: the detection chain has to fit in the dedicated space in the accelerator tunnel passage.

UA9 experiment has "graduated" from a purely experimental installation in SPS to an operational prototype in LHC under the responsibility of the LHC Collimation Team. The requirements for the proton counter for the LHC are more demanding in regards to radiation hardness: the neutron flux will be around 10^{15}/cm^2 in the beam pipe, 10^{13}/cm^2 at one meter of it.

3 The CpFM detector chain

3.1 Description of the detection chain

As the detection chain has to be placed directly inside the accelerator beam pipe, it prevents the use of semiconductor or gaseous detector which, together with their readout electronics, are not vacuum compatible. Therefore, the detector chain is composed by a radiator producing light when a particle passes through it, readout by a photodetector that is placed outside of the beam pipe.

As scintillators cannot survive at high rates of radiation, we chose to use Quartz (Fused Silica). that can support it being damaged to a lesser extent. The photodetector used to detect the Cherenkov light emitted by the Quartz might have the following characteristics: resistance to the radiations (section 2) good sensitivity for wavelengths from 400 to 800 nm (range of the Cherenkov emission), high gain (at least 10^5), short rising time: 1–2 ns and short recovery time < 10 ns. The Silicon Photomultiplier (SiPM) which was a very promising candidate (compact, robust, high gain, good timing properties) was still too sensitive to the radiations [12, 13] (the best one supported a fluence of 10^{12} neutrons/cm^2 which did not let us any safety margin when we started the detector development). Therefore, we chose a radiation- hard photomultiplier (PMT) with good timing properties and high gain connected to the Quartz radiator by means of a fibers bundle that places it away at 1 m from the beam pipe.

The conceptual drawing of the detector we developed called Cherenkov detector for proton Flux Measurement (CpFM) is shown on figure 3; the detection chain is inserted inside the beam pipe owing to a motorized support that keeps the radiator to parking position when the CpFM is not used in order to not restrict the machine aperture.

2017 JINST 12 P04029

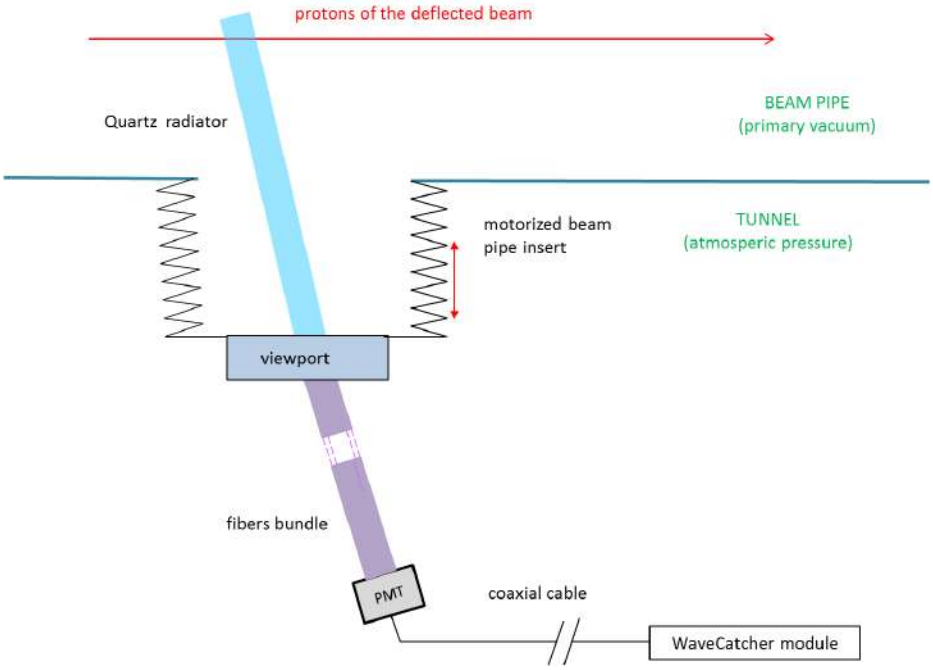

Figure 3. Conceptual drawing of the CpFM composed by 2 parts: the first one in the primary vacuum of the beam pipe is made of the Quartz radiator. At the outside of the beam pipe a Quartz optical fibers bundle will transport the light to the photodetector. The signal produced by the detector will be read out and stored by the Wavecatcher electronics (see section 3.1.4).

3.1.1 The radiator

Fused Silica, a synthetically made Quartz, is a very pure material with minimal inclusions (it will be called "Quartz" hereafter). It was chosen as a radiator because of its high resistance to radiation. It can be shaped to serve both as Cherenkov radiator and as light guide transmitting the produced photons to the PMT; in the CpFM case, a bar shape is the basic configuration from which we began our study. Cherenkov photons produced by proton passing through the Quartz bar are trapped inside it by total internal reflection.

In order to minimize the light losses, the refraction indices of the Quartz bar (figure 4), the optical fibers and the PMT window have to match and the photodetector has to be sensitive to the detection of single photons.

Depending on the bar length, the photons will bounce (figure 5) several tens of time before exiting the bar, therefore the internal reflection coefficient must be close to one (equal or larger than 0.9999 if we require than 90% of the photons reach the end of the radiator).

Owing to the important work performed for the R&D of the PID system for the BABAR [14] and SuperB experiments, as well as irradiation studies [15] results, we have chosen the fused silica Spectrosil 2000 as the radiator of the CpFM with very stringent requirements: the surface flatness was specified to be better than 100 nm and the quality of the polishing of 100 nm (RMS) in order to maximize the internal reflection coefficient.

2017 JINST 12 P04029

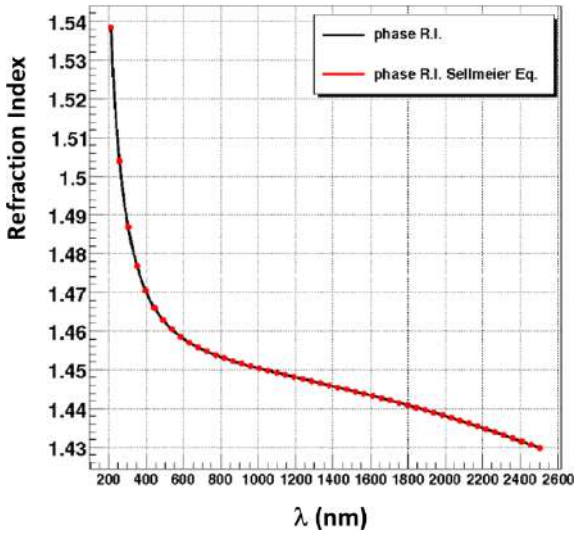

Figure 4. Wavelength dependence (nm) of the refraction index of fused silica (computed values from the Sellmeier equation [16]).

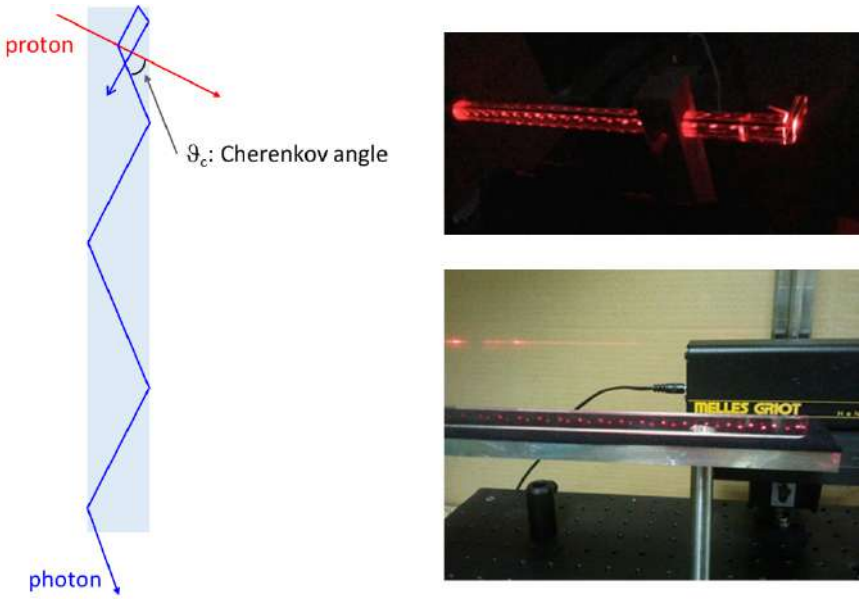

Figure 5. Left: Cherenkov photon paths inside the Quartz bar. Right: laser beam bouncing in the bar.

3.1.2 The optical fiber

When the Quartz radiator bar is inserted in the halo beam, its end will be at 17 cm of the beam pipe. When it is retracted in parking position, it will be at 43 cm, therefore, the PMT would have to stand a fluence of 10^{14} neutrons/cm^2 and very high dose (4 kGy estimated) over the year as it is placed just at the bar output. In order to decrease the impact on the PMT, and also to test a configuration that could be used in the LHC, we decided to put the detector 1 m away from the beam pipe. The light is then transported through an optical fibers bundle from the bar end to the PMT window.

2017 JINST 12 P04029

Standard plastic fibers are not suitable for this purpose because they are not immune to radiations [17–19], therefore we chose fibers made of pure Fused Silica (Heraeus Fluosil) with a Tefzel coating. To keep the photons inside the fiber by total internal reflection, the cladding was carefully chosen with a refraction indice close to the Quartz's, which is composed of Fluorine doped Fused Silica. Figure 6 shows the attenuation as a function of the light wavelength of this fiber which is under 100 dB/km for the wavelength range of interest (400 to 800 nm).

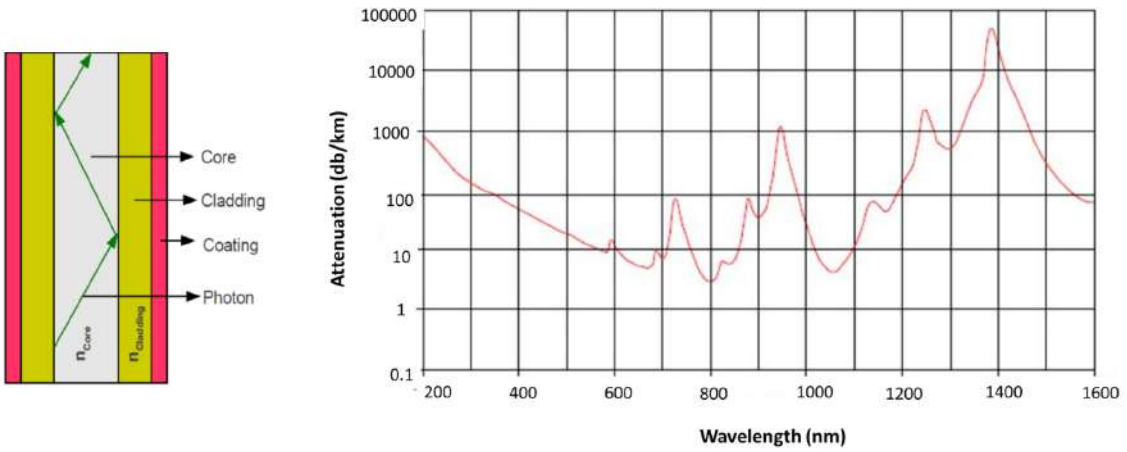

Figure 6. Left: sectional drawing of a fiber — Right: typical fiber attenuation as a function of the wavelength [20].

As the numerical aperture of this fiber is 0.22, photon have to enter the fiber with an angle smaller than the acceptance angle (figure 7) of 8° to profit from internal reflection and reach the end of it.

3.1.3 The photodetector

The PMT chosen for the CpFM has to work in a very radiation hostile environment (10^{12} neutrons/cm^2 at one meter of the beam pipe), with a good sensitivity for wavelengths from 400 to 800 nm, a minimum gain of 10^5, and good timing properties (rising time: $\leqslant 2$ ns and recovery time < 10 ns). Its window refraction index has to match the one of the Quartz fibers that bring the light from the Quartz bar.

As for the radiator and the fiber, it is the radioactive environment that fixes the choice of the PMT: compact PMTs with metal channel dynodes cannot be used because of their coating made with resins that are not radiation-resistant, therefore the PMT has to be only made of glass and metal. We used the results of the studies performed for the upgrade of the luminosity monitor of ATLAS [21] which show the effect of neutron and gamma radiations on the gain, the quantum efficiency and the dark current of PMTs, to select two detectors: HAMAMATSU R762 and R7378A, both with a Quartz window that does not show loss of transmittance due to the coloration of the glass when exposed to radiation, unlike Borosilicate glass [22].

The table 1 shows the characteristics of the two chosen PMTs. The results of the measurement of the gain are shown on figure 8.

2017 JINST 12 P04029

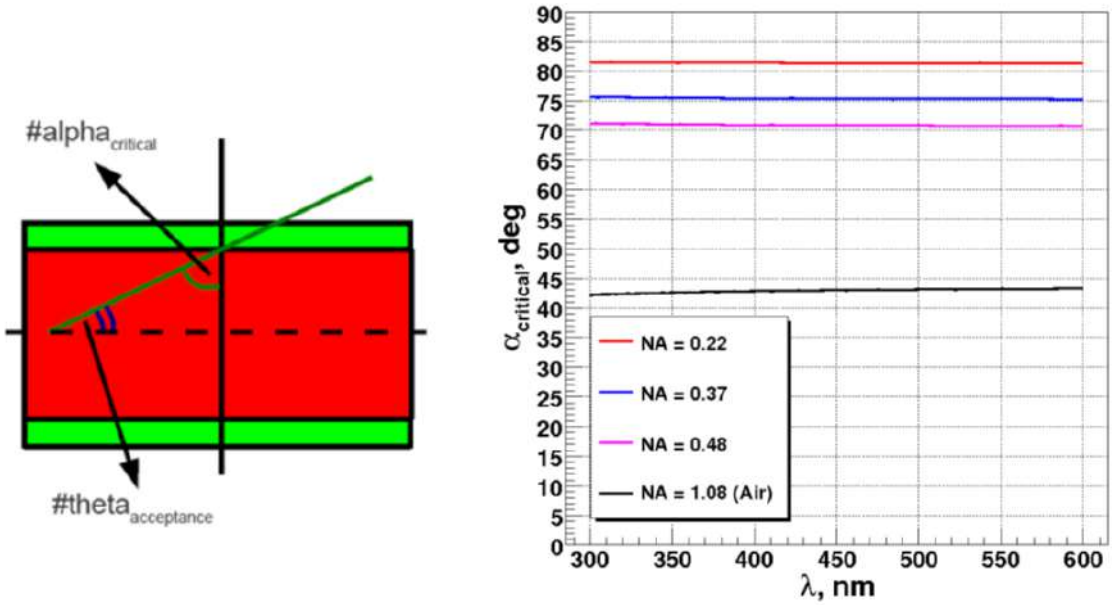

Figure 7. Left: critical (α) and acceptance (ϑ) angles of the photon track inside the fiber — Right: computation of the critical angle as a function of the photon wavelength for different numerical apertures.

Table 1. Main characteristics of the PMTs R762 and R7378A [data sheets].

	R762		R7378A	
Window material	Synthetic Silica		Synthetic Silica	
Bialkali Photocathode diameter (mm)	15		22	
Photocathode material	Bialkali		Bialkali	
Typical gain	10^6		2.10^6	
Typical dark current (nA)	1		1	
Maximum sensitivity (nm)	420		420	
Typical Radiant Sensitivity (mA/W)	85		85	
Rising time (ns)	2.5		1.5	

The PMT stability will be checked during each SPS technical stop (dark current and response under illumination) every 3 months. As the CpFM will be put inside the beam only 3 times per year (periods of 10 to 24 h), the lifetime of the PMT will not be affected by problem of accumulated charge. In case the PMT suffers damages due to the radiation, it would be replaced on a one-year time scale, as it will be accessible and it is relatively inexpensive.

The measurements of the PMTs response as a function of the incident light flux (figure 9) were performed with a blue LED (405 nm ±2 nm) biased with a pulse generator producing a light pulse with a duration of 10 ns at a frequency of 43 kHz in order to simulate the SPS revolution frequency. The incident flux is determined by a calibrated PMT.

3.1.4 The readout electronics

The PMT signals are readout by waveform digitizers called WaveCatchers [23] triggered by the UA9 trigger signal generated by a Static Trigger Unit using the revolution frequency signal and

2017 JINST 12 P04029

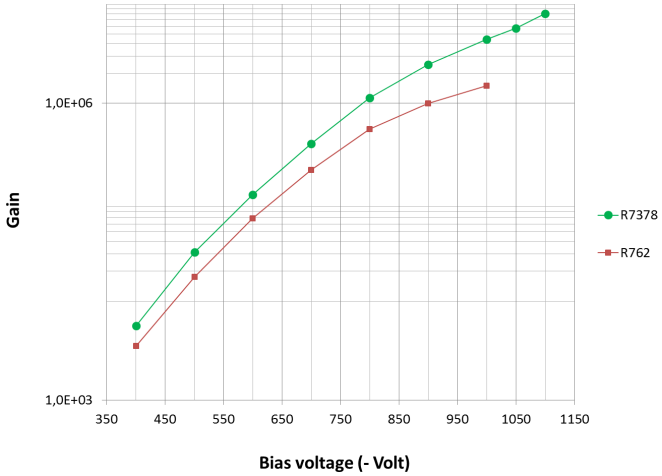

Figure 8. Measured gain of the PMT R762 and R7378A as a function of their bias voltage at room temperature.

the RF clock signal of the SPS (figure 10). The WaveCatcher family of modules, based on the SAMLONG [24] chip, offers a signal bandwidth of 500 MHz, and permits sampling the analog signal between 400 MS/s and 3.2 GS/s, then converting it into digital over 12 bits.

Different versions of this system (figure 11) were used either for the beam tests of the CpFM, either for the final installation in the SPS: USB-powered 2-channel version, 8-channel version (desktop module) and the 16-channel version. All channels can participate in sophisticated triggers and feature extraction of the signals (baseline, peak, charge, timing. . .) is performed on-board in real time.

The boards are interfaced to computers via USB. Dedicated software and libraries permit an easy handling of the boards and modules, particularly in the case of test beam setups.

In the case of UA9, this allowed the developers to integrate the control and acquisition software (figure 12) of the WaveCatchers inside the global DAQ system, thus enabling the synchronization of data readout and consequently that of the signals recorded among all subdetectors.

As the WaveCatcher electronics is based on standard components, especially FPGAs, it is not tolerant to radiations. It thus has to be located in a low radiation area, 40 meters from the PMTs. In order to transport the PMT's signal to the readout module, we used a low attenuation shielded coaxial cable (CKB50) that fulfills the criteria for the selection of electrical cables and equipment with respect to fire safety and radiation resistance at SPS.

3.2 Simulation of the CpFM

Detailed simulations based on Geant4 [25] were performed in order to optimize the detector geometry. Cherenkov photons (N_γ) were generated in the radiator, along the proton path with wavelength-dependent optical properties of Fused Silica (refractive index and free path length [14]). The propagation of the generated photons takes into account the quality of the radiator surface as well as its bulk properties (inclusions concentration). The quantum efficiency (Q_ε) and collection efficiency (C_ε) of the PMT with its Bialkali photocathode were taken into account. The coupling

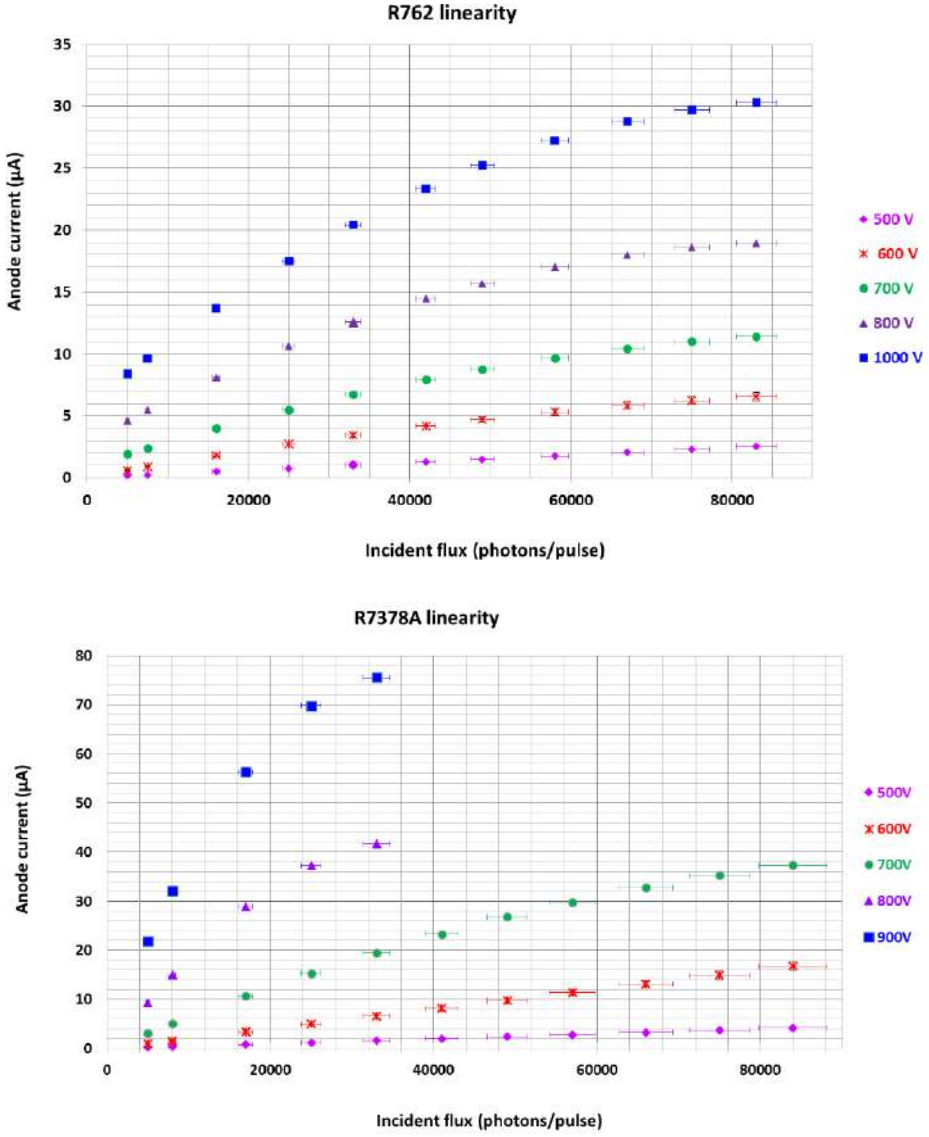

Figure 9. Anode current as a function of the incident flux of photons, at different bias voltages for the PMT R762 (top) and R7378A (bottom).

between the radiator and the photodetector or the fibers bundle was considered as perfect, therefore the simulation gives an upper bound of the number of produced photoelectrons.

The number of photoelectrons ($N_{p.e.}$) is given by:

$$N_{\text{p.e.}} = N_\gamma \times Q_\varepsilon \times C_\varepsilon \, .$$

Fifteen different geometries were studied, from the simplest one to very elaborated as the one shown in figure 13. It consists of a single piece of Quartz with 3 parts: a square bar placed inside the beam pipe crossing the proton path, a cylindrical plate that plays the role of a viewport connected to the flange, and a pyramidal shape that assured the connection with the fibers bundle. Owing to this geometry, there are no optical losses at the interface between the radiator and the viewport.

2017 JINST 12 P04029

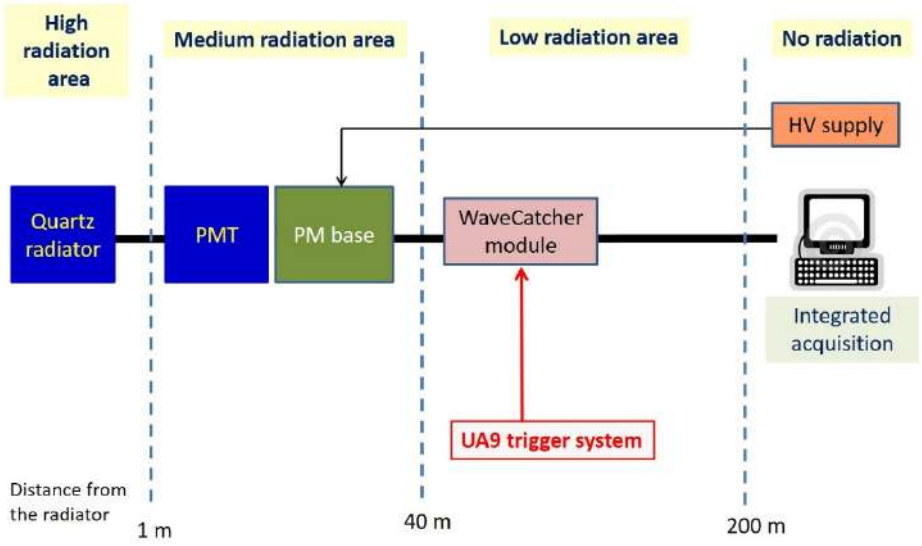

Figure 10. CpFM chain from the radiator to the acquisition system.

Figure 11. Left: 16-channel WaveCatcher board — Middle: 2-channel USB and 8-channel WaveCatcher module — Right: crate composed of 6U custom-board which can be integrated in a small crate controlled by a dedicated board in order to reach up to 64 channels.

Figure 13-right shows the distribution of the number of photoelectrons (p.e.) per incoming proton on the Quartz bar produced at the PMT photocathode output for a direct coupling between the radiator and the PMT.

Despite the large number of produced photoelectrons, this geometry had to be abandoned due to its manufacturing complexity (cutting of the different shapes in a single Quartz piece and their polishing).

The second most promising geometry, called hereafter L-bar, is shown on figure 14: the incoming proton hits the short leg of the L-bar producing Cherenkov photons which propagate toward the end of the radiator cut at 47° (Cherenkov angle for Quartz). Depending on the thickness of the bar (3, 5 or 10 mm), the output flux can be as high as 150 p.e. proton.

In order to estimate the background, we studied a configuration with 2 or 3 bars (figure 15). As shown on figure 16-left, the crosstalk between channels is negligible. When the outer bar of the

2017 JINST 12 P04029

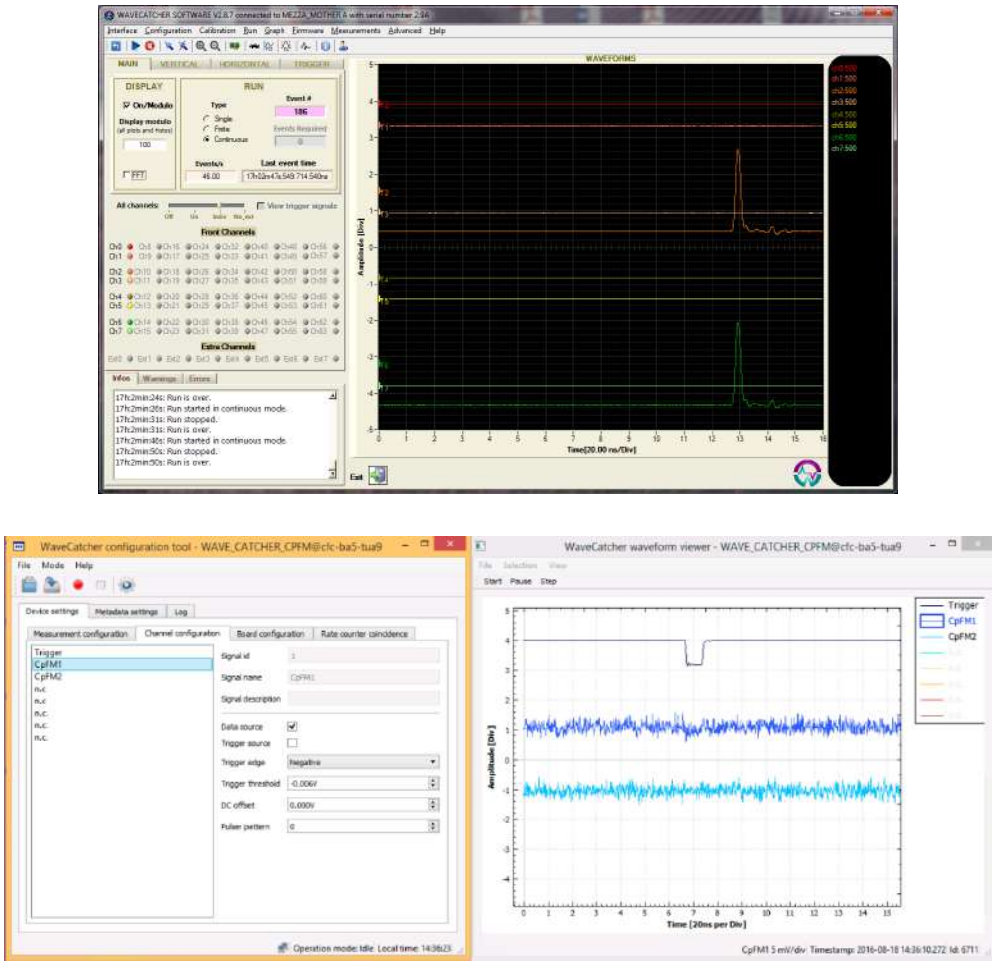

Figure 12. Graphical user interface of the WaveCatcher software in local mode (top) and in the UA9 SPS DAQ mode (bottom).

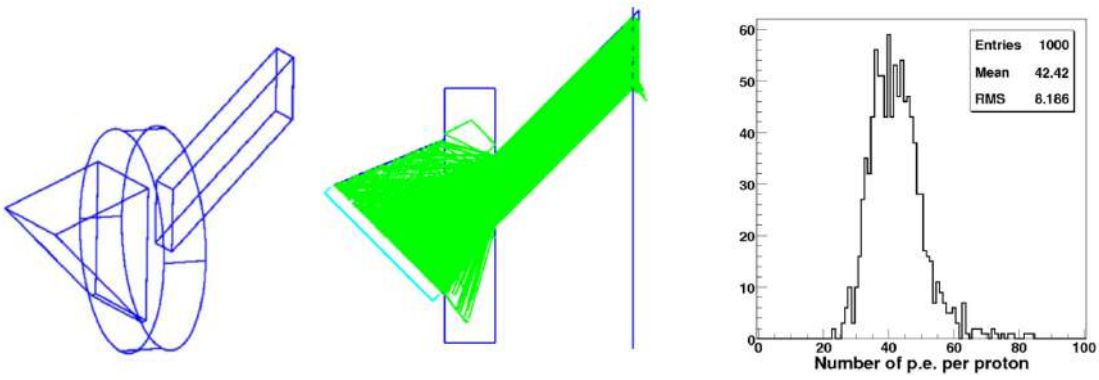

Figure 13. Left: 3 dimensional drawing of the CpFM first geometry — Middle: Cherenkov photons paths (green) inside the Quartz radiator — Right: distribution of the number of p.e. per incoming proton produced at the PMT photocathode output for a direct coupling between the radiator and the PMT.

2017 JINST 12 P04029

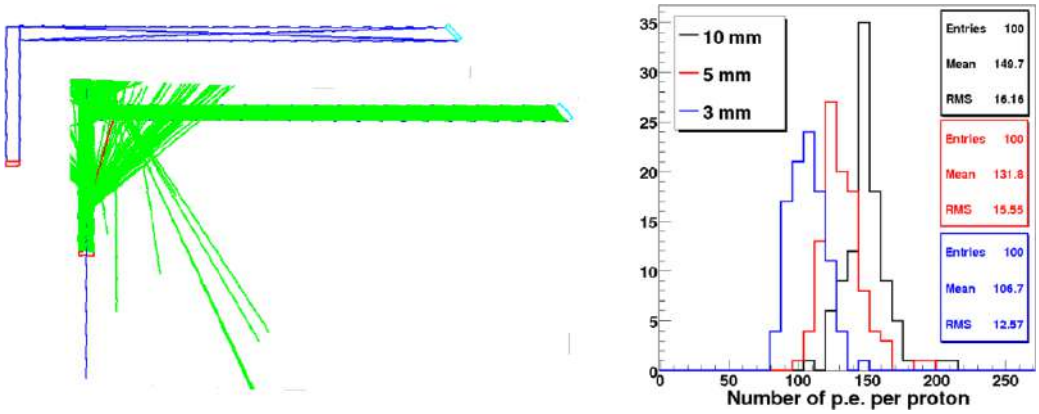

Figure 14. Left: drawing of the L-bar geometry. The proton interacts inside the short leg of the L (30 mm long) Cherenkov photons (in green) are internally reflected toward the end of the long L leg — Right: distribution of the number of p.e. per incoming proton produced at the PMT photocathode output for a direct coupling between the radiator and the PMT for 3 different Quartz thickness (3, 5 and 10 mm).

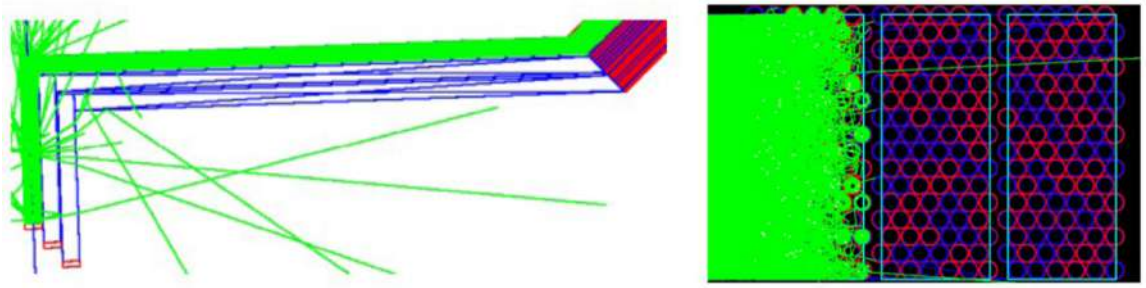

Figure 15. Left: CpFM composed of 3 L-bars (5 mm thickness) attached to their fibers bundles (96 fibers 4 m long) — Right: spatial distribution of the photons at the fibers output when only one bar interacts with the proton beam.

CpFM is moved inside the deflected beam, the inner bar only interacts with background particles, its signal can therefore be subtracted.

The figure 16-middle shows the effect of the bundle composed of 96 fibers with a length of 4 m: the number of p.e. per incoming proton produced at the PMT photocathode is divided by a an order of magnitude with respect to the number produced when the coupling between the bar and the PMT is direct.

The L-bar with a thickness of 5 mm was the optimized geometry for the measurement of the deflected flux; however, due to production problems (see section 5.1.3), it had to be replaced by a straight bar (called "I bar").

Results of the simulation of an I-bar with a thickness of 5 mm is shown on figure 17: both direction of the proton beam (normal and inverse) give the same results: with a direct coupling between the bar and the PMT, the mean value of the p.e. distribution is 28, 5.3 time less than with the L bar configuration which is consistent with the ratio of 6 between the thickness of the quartz crossed in the L bar (30 mm) and the one of the I bar (5 mm). The Polar angle distribution of Cherenkov light is almost flat from 0° to 60° region. When the bar is connected to the bundle, only

2017 JINST 12 P04029

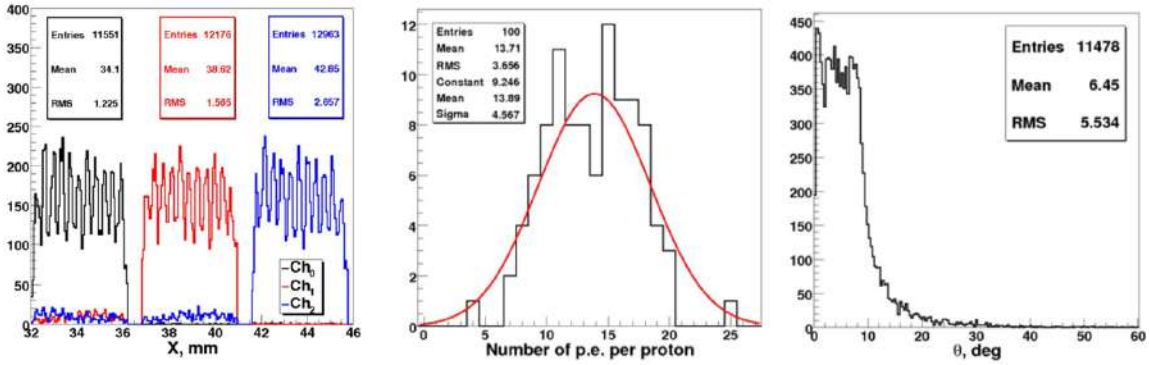

Figure 16. Left: x-distribution of the photons (arbitrary units) arriving on the PMT photocathode after the bundle. The 3 colors correspond to the protons entering different bars. The black distribution corresponds to the protons entering the most outer bar, the red one to the middle bar, the blue one to the most inner bar — Middle: distribution of the number of p.e. per incoming proton produced at the PMT photocathode after 4 meters of fibers bundle — Right: polar angle (with respect to bundle axis) distribution of Cherenkov photons (the angular cut due to numerical acceptance of the fiber).

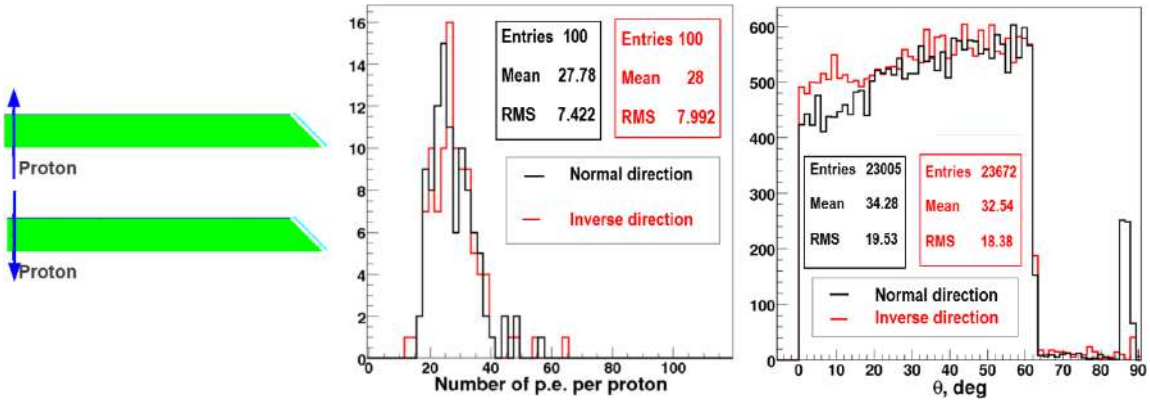

Figure 17. Left: drawing of a Quartz I-bar — Middle: distribution of the number of p.e. per incoming proton produced at the PMT photocathode in direct coupling — Right: polar angle (with respect to bundle axis) distribution of Cherenkov photons.

the photons within the numerical aperture of the fiber ($\sim 8°$) can be captured by the fibers. This limitation together with the fiber fill factor (the active area is not equal to the total one due to dead spaces between the fibers inside the bundle packing) make the mean value of the p.e. drops down to 2.3.

The table 2 shows the simulation results of the bars with L and I shape when directly coupled to the PMT or via the 4 meters fibers bundle.

The final CpFM as shown on figure 18 is composed of a first channel for the measurement of the number of protons populating the deflected halo superimpose to the background and of a second one which will measure the background.

2017 JINST 12 P04029

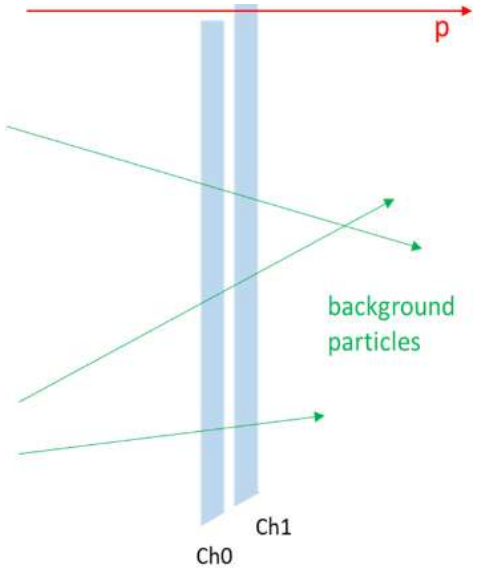

Figure 18. 2-channels CpFM. The channel 0 composed will measure the background as the channel 1 will measure the number of deflected protons + background.

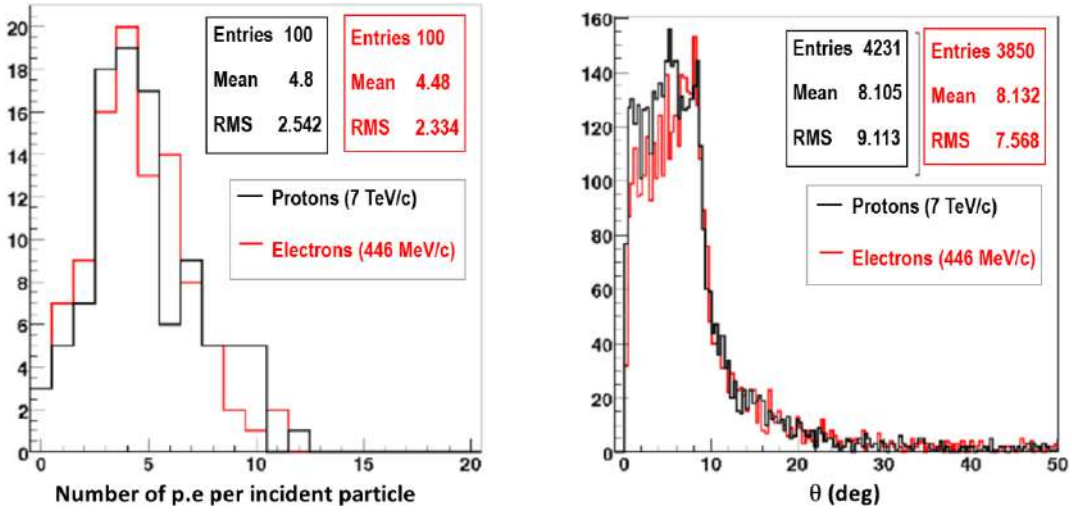

Figure 19. Left: Geant4 simulation of the distribution of the number of photoelectron produced at the photocathode output per incident particle (proton in black, electron in red) for Quartz bar coupled to a 4 m length fibers bundle — Right: distribution of the polar angle (with respect to the bar axis) of Cherenkov photons.

4 CpFM prototype: proof of principle

We built a simplified CpFM prototype and tested it in the BTF facility of the INFN-LNF in Frascati with 446 MeV/c electrons (bunch of 10 ns). It was checked by simulation (figure 19) that the signal produced by the CpFM under a 7 TeV/c proton beam (LHC conditions) and the BTF 446 MeV/c electron beam were similar.

The prototype (figure 20) was composed of all the CpFM components chosen for the SPS [26]; it consists of the assembly of a square section Quartz bar ($100 \times 5 \times 5\,\mathrm{mm}^3$), a home-made

Table 2. Comparison of the simulation results of the L and I Quartz bars in direct coupling to the PMT or via the 4 meters fibers bundle.

Investigated issue	Relevant parameters	Results (number of p.e /proton produced at the PMT photocathode)
Geometry design proposal "L"-shaped bars	"L"-shaped bar Thickness: 5 mm	131.8
Effect of the bundle	"L"-shaped bar Thickness: 5 mm Fibers bundle: 96 fibers, 4 m long	13.9
Alternative design "I"-shaped bar	"I"-shaped bar (straight bar) Thickness: 5 mm	27.8

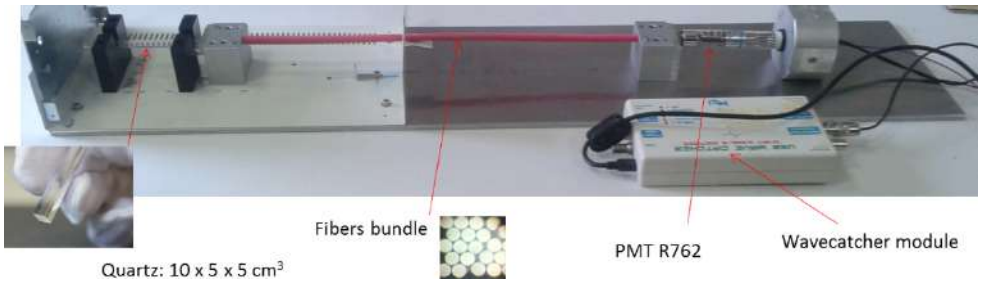

Figure 20. Prototype of the CpFM.

Quartz fibers bundle (25 fibers 120 mm long), a PMT R762, a low attenuation cable of 40 m and a WaveCatcher module.

As the Quartz bars should not be touched to avoid any loss of the total reflection of the light, a special mechanical system, ultra-vacuum compatible, has to be designed and built to hold it. Also, the optical grease that would darken in the SPS tunnel under the radiation background, cannot be used to optimize the optical couplings. Therefore, particular care should be given to the qualities of the interfaces between the different optical components: Quartz to fibers, fibers to PMT window to get the largest number of photons to the PMT photocathode.

The most important property of the CpFM geometry, its optimum angle with respect to the incident particle in the Quartz bar, was checked; the simulation predicts that, when intercepting particles at 90 degrees, the photons exiting from the bar have the distribution shown in figure 21. The number of photons injected into the fibers bundle reach its maximum at 47° at the bevelled end of the radiator which corresponds to the Cherenkov angle (for ultra-relativistic particle) in Fused Silica. Due to the small numerical aperture of the fibers, all the photons arriving with an angle larger than 8° are lost. Therefore we had only a small margin to align fibers to the photons directions. To compensate for the photon emission angle, the bar has to be inclined at 45° with respect to the direction of incoming particles.

We compared, with the BTF beam, the CpFM response for an inclination of 45° with the beam and another one at 90° (figure 22) and checked that "45° configuration" was the optimum one.

2017 JINST 12 P04029

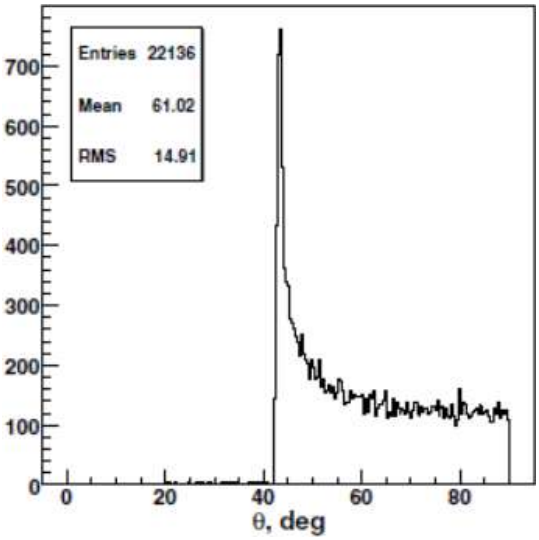

Figure 21. Distribution of the polar angle of the Cherenkov photons emerging from the read-out surface of the Quartz bar when it intercepts at 90 degrees electrons of 450 MeV. Cherenkov light generation and propagation are simulated using GEANT4.

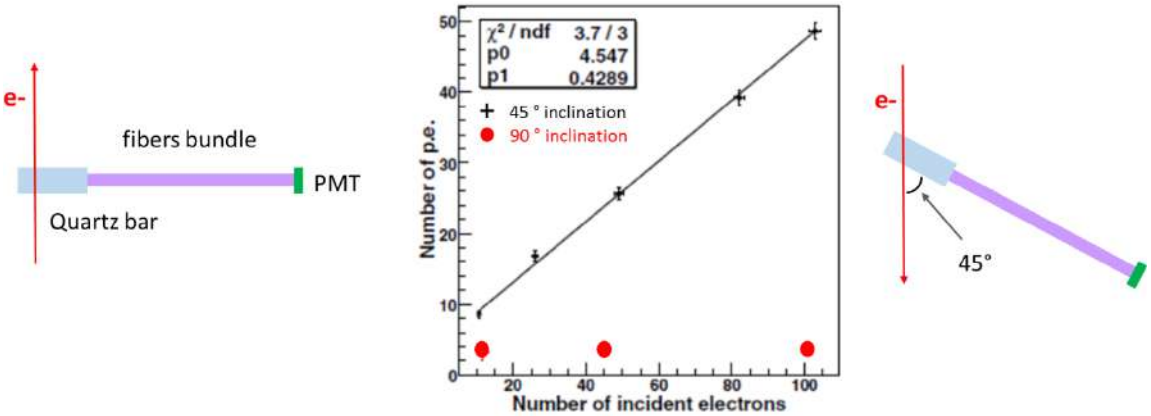

Figure 22. Measurement of the CpFM response as a function of the incident electron flux for 2 configurations: the Quartz bar at 90° from the beam (red dots) and the bar at 45° (black crosses).

When the electron direction is at 90° with the bar, the light produced arrives with an angle which does not match the small angular acceptance of the fibers therefore it is not transported to the PMT.

We measured during this beam test that the attenuation of the signal inside the 40 m cable is around 10% (figure 23) which confirms the choice to not use a preamplifier which would not stand the radiation level at this place near the beam pipe.

The Geant4 simulation of the response of the Quartz bar connected to the PMT predicts a mean value of 62.5 for the number of photoelectrons produced at the photocathode output per incident electron (figure 24 left). Using the CpFM prototype, we measured the integral of the signal generated by the particles traversing the Quartz bar (charge). This distribution is reported in figure 24 right: it shows a good separation of the peak corresponding to one incident electron from

2017 JINST 12 P04029

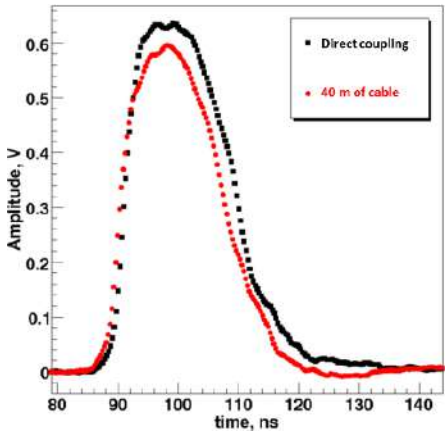

Figure 23. CpFM prototype signal response to 1 electron when the PMT is directly connected to the WaveCatcher module and when a 40 m long cable is inserted between the PMT and the module. The 2 curves had been superimposed (the signal after 40 m of cable arrives 150 ns after the direct one).

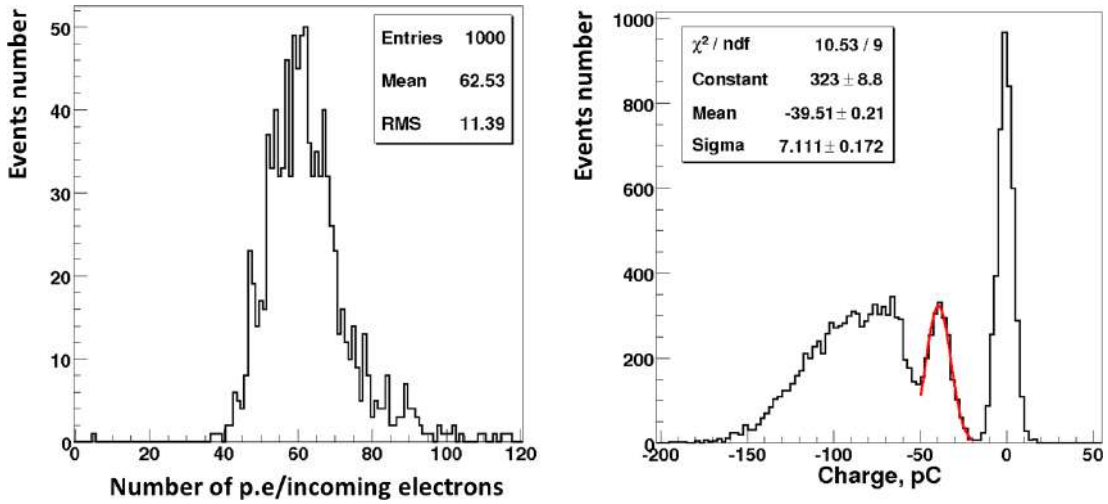

Figure 24. Left: simulation of the distribution of the number of photoelectrons produced at the photocathode output per incident electron on the bar directly coupled to the PMT. Right: histogram of the charge (pC) of the PMT measured with low intensity electrons beam (between 1 and 4 electrons/bunch).

the pedestal. Knowing the gain of the PMT, we can evaluate that the interaction of one electron inside the Quartz bar generates on average 57.4 photoelectrons, which is in good agreement with the simulation. After data analysis we deemed that this 10% of difference was due to the optical losses at the interface Quartz/PMT.

5 The CpFM for SPS

The first implementation of the CpFM detector was prepared to be integrated in the UA9 experimental setup in SPS. This detector was built with two objectives: 1 — provide useful data to UA9 in order to characterise its crystal-collimation prototype system and 2 — built a prototype system

2017 JINST 12 P04029

compatible as much as possible with LHC requirements in order to point out possible problems and needed technological developments.

5.1 Building of the CpFM for the SPS, technological problems and solutions

5.1.1 The PMT and its divider circuit

If we consider that the number of protons populating the deflected beam halo will not exceed 200, the value of the number of Cherenkov photons created inside the Quartz bar and reaching the PMT at the end of the fibers bundle will be between 5000 and 10000. Both PMTs, R762 and R7378A are linear over this range but the R7378A which is smaller was chosen for the readout of the radiator's CpFM.

As no special divider circuit is needed to improve the linearity of the detector, we built the standard circuit (figure 25) advised by HAMAMATSU for this device. All components (PCB, resistors and capacitors) are radiation-hard except the socket which is made of metal and plastic whose radiation hardness was not tested. As the PMTs will be placed on the SPS tunnel floor, at about 1 meter from the beam pipe, they are placed inside light-tight metallic boxes that can protect them from electromagnetic perturbations.

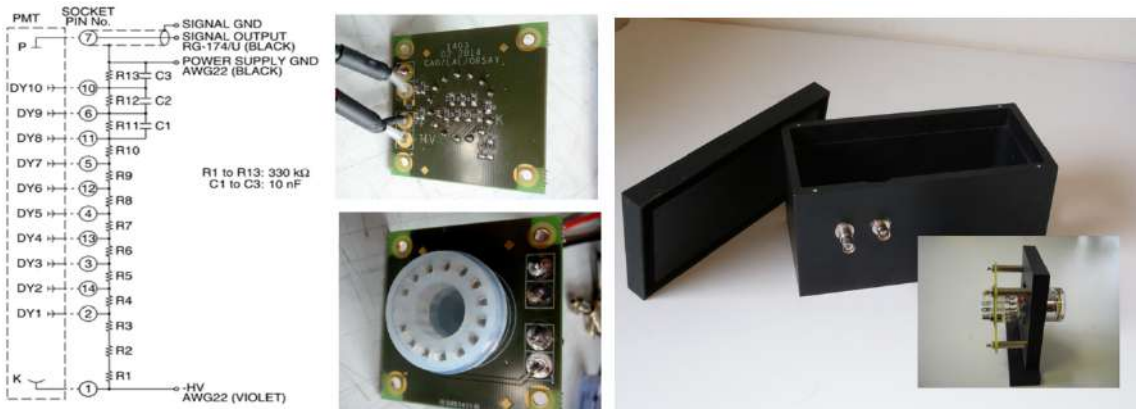

Figure 25. Left: divider circuit diagram for the R7378A (from the PMT datasheet) — Middle: the compact divider card — Right: the light-tight shielded box that hosts the PMT connected to its divider card.

5.1.2 The fiber bundle

The light guide (figure 26) that collects the photons produced inside the Quartz bars is composed of 2 4-meters long independent bundles made of 100 fibers each (the PMT will be put on the floor, one meter from the output of the quartz bars but as the quartz fibers are very fragile and cannot be bent at a radius smaller than 400 mm, 4 meters are needed to connect the radiators and the photodetectors).

As the SPS tunnel is constantly lit, the fibers are protected from the background light by a flexible stainless steel pipe. The final assembly is very fragile, for this reason before installation it was checked that less than 2% of the fibers were broken, according to initial specifications.

5.1.3 The Quartz bars

Two producers were contacted to produce the Quartz bars for the detector to be installed in the SPS.

2017 JINST 12 P04029

Figure 26. The 4 m bundles composed of 100 fibers each. The ends of the bundles match the shapes of the Quartz bars (rectangle) and of the PMT window (round).

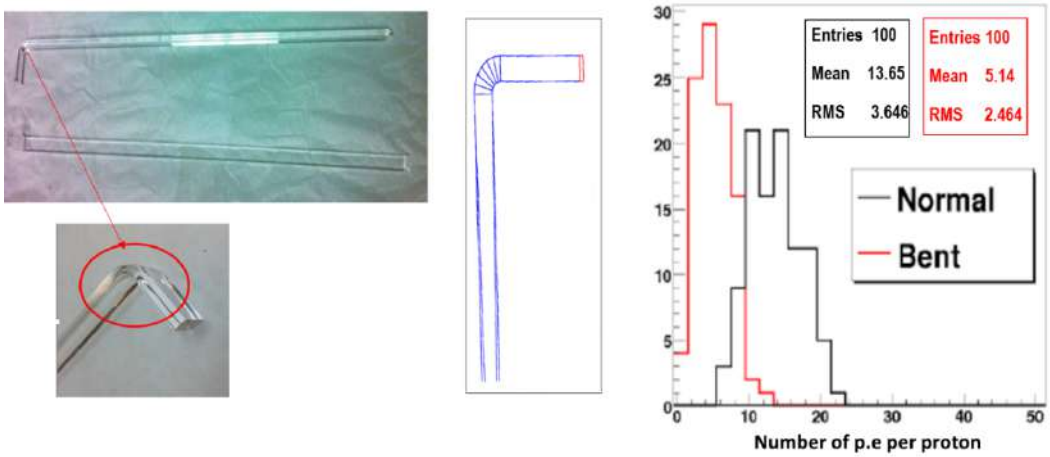

Figure 27. Left top: pictures of the defective L-shape Quartz bars called "bent" bars — Left bottom: L bar with right angle — Right: distribution of the number of photoelectrons produced at the PMT photocathode output after 50 cm long fibers bundle (160 fibers) simulated with the L-shape bar (black histogram) and the bent bar (red histogram).

The L-shape Quartz bars we received from the first producer were defective: the angle between the two legs of the L was not close enough to 90 degrees and the corner of the "L" was bent rather than sharp (figure 27). The effect of this defect was simulated with Geant4: the distribution of the number of photoelectrons produced at the PMT photocathode output with the two bars connected to the PMT window by a fibers bundle shows a decrease of the detected signal by a factor of 2.6 with the bent bar. Therefore, these bars were not used.

The second producer succeeded in cutting the bar with a right angle.

We also ordered straight bars (that we called "I bar") that can be polished easily, as a backup solution. As we were not equipped to measure the polishing quality of the bars, we performed tests at BTF (figure 28) in order to compare all the bars and chose the best candidate for the installation.

The Quartz bars are held by holders made in Teflon that simulated the flange. They are touched only at their corners at a few positions in order to minimize the absorbing regions. The CpFM placed on a translation stage was moved perpendicularly to the beam in order to intercept it at different positions along the bar length.

2017 JINST 12 P04029

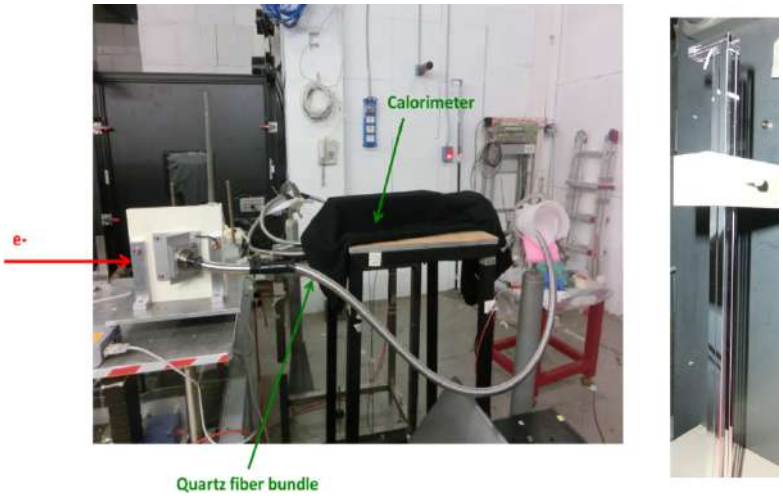

Figure 28. Left: CpFM tests setup at BTF — Right: L bars attached to a support made in Teflon that simulates the flange.

The L and I bars are compared in figure 29 which shows the number of produced photoelectrons as a function of the beam impact position on the bent bar. The L bars exhibits a larger signal in the first part of the scan, corresponding to the beam crossing the short leg of the L (30 mm thick), while the signal is reduced by a factor 2 when electrons cross the long leg of the L (5 mm thick). If all the photons created inside the short leg of the L bar were transmitted to the end of the radiator, the value of this ratio would be equal to 6. As this ratio is only 2, we can assume that photons produced in the short leg of the L are lost rather than internally reflected to the end of the bar because of a bad quality of the Quartz polishing. We also observed an increase of the signal when the electrons impinge closer to the end of the bar: this shows that the quality of the polishing is not good enough, as part of the photons created far from the end of the bars quit it. For positions larger than X=550 mm, data are affected by an under estimation of the number of electrons interacting in the calorimeter since the Teflon support holding the bar shielded a part of the calorimeter.

From purely geometrical considerations, the I bar should give less signal than the L one at its edge (since electrons cross 5 mm of Quartz instead of 30 mm) and identical signal along their length (where both bars are 5 mm thick). However we measured that the I bar has a signal 5 times larger than the L one on the flat part of the curves. This observation confirmed that the polishing of the L bar is of bad quality: the manufacturer explained that the asymmetrical shape of the bar caused unwanted vibrations inside the polishing machine, compromising the final quality.

Given the time needed to find a technology providing a better set of L bars and in order to avoid to postpone the installation of the detector in SPS, it was decided to use I bars as Cherenkov radiators.

5.1.4 The mechanical integration of the bars

5.1.4.1 The CpFM tank

The tank (figure 30) that hosts the CpFM was built following a design already used in the SPS for several devices and its contribution to the impedance of the machine was studied by the UA9

2017 JINST 12 P04029

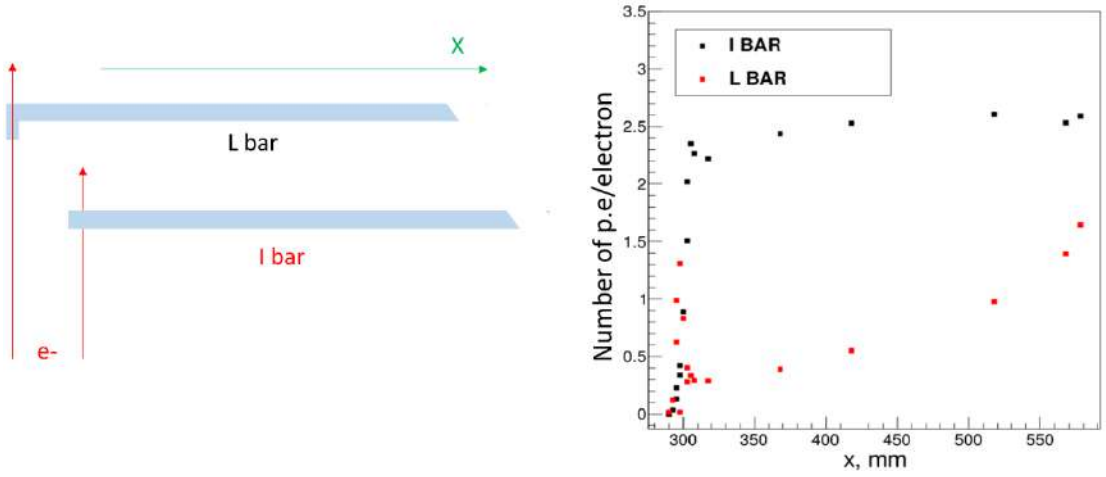

Figure 29. CpFM signal (number of photoelectron/e-) as a function of the impact position of the electron in the Quartz bars: I bars (black points) and one L bar (red points).

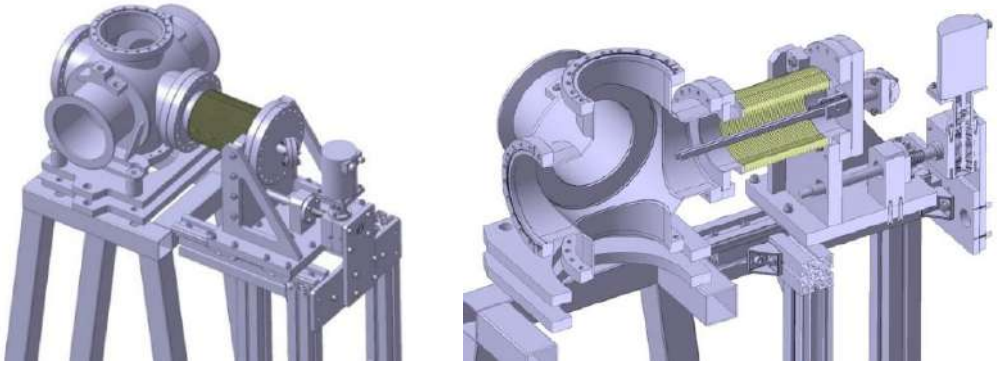

Figure 30. Drawing of the CpFM tank.

team [27]. The Quartz bars are inserted inside the beam pipe by compressing a bellow fixed to a slide moved by a trapezoidal screw actuated by a radiation-hard stepper motor.

5.1.4.2 Brazing of the bars with the flange

In order to maximize the number of Cherenkov photons reaching the PMT, we wanted to limit the number of interfaces between the components of the CpFM by passing the bars through the flange (figure 31-left) closes the tank. The specifications for the brazing of the bars to the CF150 stainless steel flange were very demanding: the optical features of the fused silica bar has to be preserved (no change in the refractive index), the interface surface between the Quartz and the flange has to be either reflective either the smallest possible in order to minimize the light losses, the assembly should be Ultra-high vacuum compatible and hermetically sealed and it has to stand a warming cycle up to about 200°C (baking is not mandatory for an installation in the SPS beam pipe but it will be for LHC).

The company in charge of the integration of the bars failed to braze them (figure 31-right); the fused silica bar seems to cool and heat faster than the stainless steel flange. This caused a stress

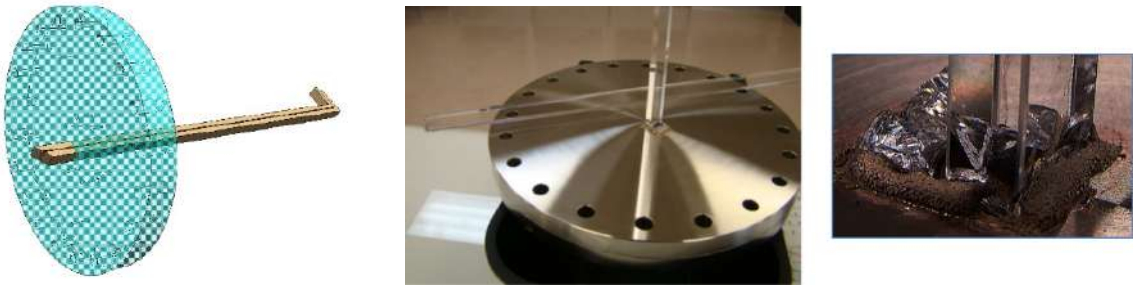

Figure 31. Left: drawing of 2 Quartz bars brazed to the CF150 stainless steel flange — Middle and right: Quartz bars broken during the brazing process.

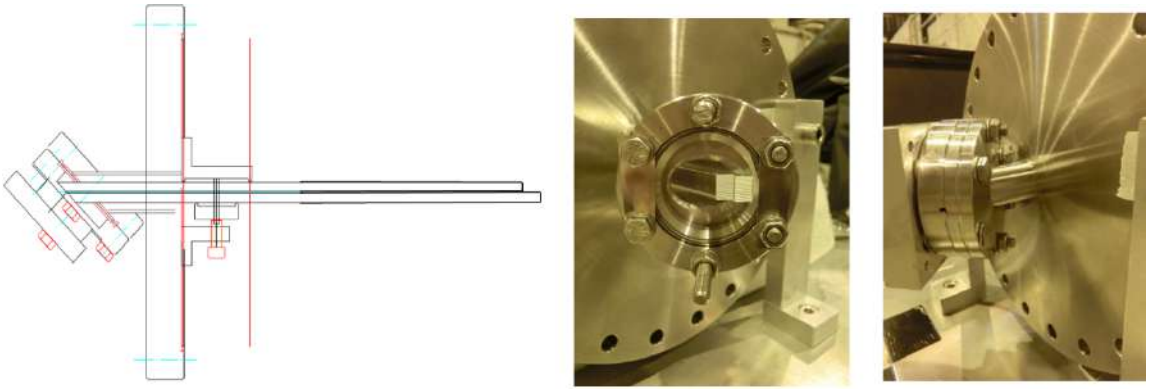

Figure 32. Left: drawing of the CpFM assembly: the bars are attached to the flange connected to an inclined viewport. Right: picture of the inclined viewport.

point for the fused silica even at the slow heating rate programmed into the furnace and caused the breaking of the bar.

As we did not find a technological solution to the brazing problem in a reasonable amount of time, we decided to use a standard Quartz viewport to transmit the light signal outside of the beam pipe. The bars are fixed by special mechanical holders inside the beam pipe with their ends touching the Quartz viewport that assures the vacuum tightness. The fiber bundle is attached to the other side of this viewport. In order to assure the transmission of the light from the radiators to the bundle as studied in section 4, the viewport has to be inclined at 47° with respect to the beam pipe (figure 32).

This additional interface between the bars and the fiber bundle decreases the amount of light transmitted to the PMTs. We studied this effect by testing an assembly composed of the Quartz bar, a glass plate of 3.85 mm of thickness that simulates a viewport of bad quality (the glass being not polished as well as the Quartz window) and the PMT. The results of the measurements (figure 33) show a reduction by a factor 2 of the signal.

5.2 Calibration of the detection chain

The CpFM chain obtained at the end of the process described in the previous paragraphs (figure 34) is composed of 2 straight 36 cm-Quartz bars: one bar is used to measure signal from the incoming

2017 JINST 12 P04029

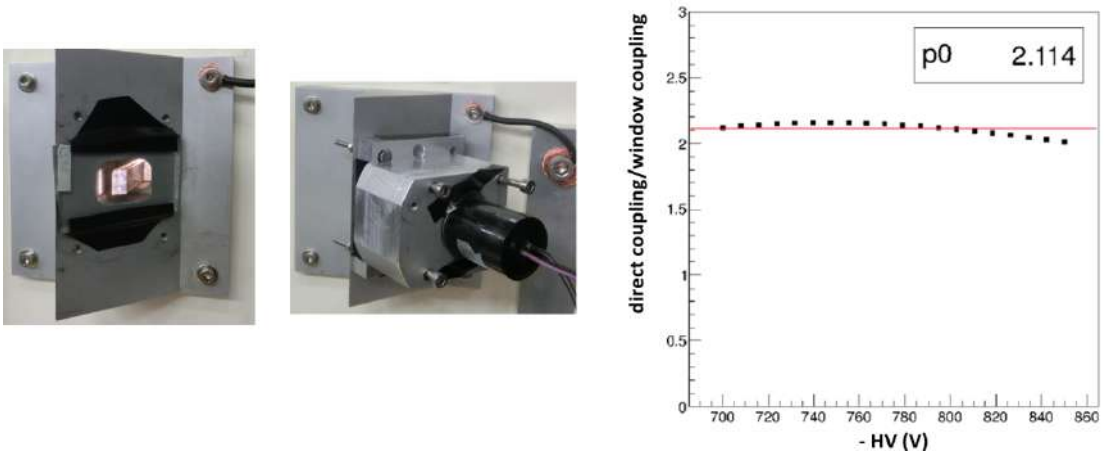

Figure 33. Left: the end of the I bars (with the 47° edge) touching the glass plate simulating the Quartz viewport then connected to the PMT — Right: ratio of the signal of the bar directly coupled to PMT to the one of the bar separated to the PMT by the glass plate as a function of the PMT bias voltage.

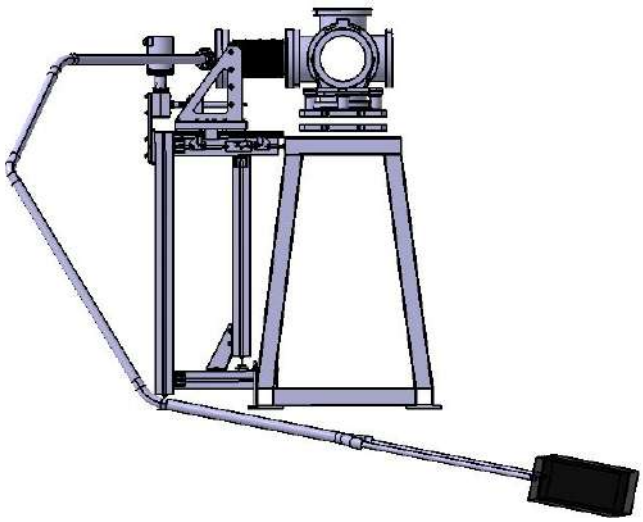

Figure 34. Drawing of the final CpFM chain.

beam and another one to monitor the background. They are fixed in order to touch the 3 mm inclined Quartz viewport that can be inserted or retracted from the beam by a motorized bellow. The window provides the optical contact between the radiators placed in vacuum and the bundle of fibers placed in air. Two radiation-hard bundles composed of fused silica/fused silica (core/cladding) fibers bring the Cherenkov light to 2 R7378A PMTs positioned at 1 meter from the beam pipe inside shielded light tight boxes. The readout of the PMT signals is performed by a 8-channel WaveCatcher module installed in a low radiation area and connected to the detector via 40 meters low attenuation cables.

The checking of the linearity of the detection chain as well as a first calibration were performed at BTF as described in [28]. It showed a calibration coefficient of 0.62 photoelectron/particle. Figure 35 shows the distribution of the number of p.e. measured by the CpFM normalized by the number of incoming electrons measured by the BTF calorimeter.

2017 JINST 12 P04029

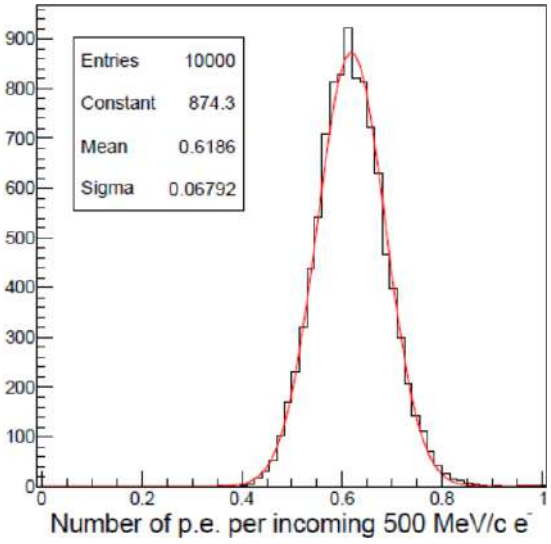

Figure 35. Distribution of the number of p.e. measured by the CpFM normalized by the number of incoming electrons.

The resolution of the CpFM is given by:

$$R = \sqrt{2}\frac{\sigma}{\text{Mean}} = 15\% \,.$$

The $\sqrt{2}$ factor is due to the fact that the measurement was performed with 200 electrons while we need to estimate the resolution for 100 protons (equivalent to 100 electrons).

The final calibration was made at CERN North Area (figure 36), in the H8 beam line with a focalized 400 GeV/c proton beam (figure 37). The CpFM measurements were made in coincidence with three trigger counters composed of plastic scintillators coupled with PMTs.

Figure 38 shows the CpFM calibration measurements results: the edge of the Quartz bar was aligned with the proton beam together with the counters. 33263 protons were selected as the events in coincidence in all the counters situated on both side of the Quartz bar. The CpFM counting 20964 events, the calibration coefficient is estimated at 0.63 photoelectron per proton, in total agreement with the measurements performed at BTF [28].

6 Operation of the CpFM in the SPS

The CpFM was successfully installed on the SPS in January 2015, 58 m downstream the crystal and upstream the secondary absorber (figure 39 & 40).

The CpFM was tested for the first time in July 2015 with a 270 GeV/c proton beam. After an initial measurement of the pedestal, the Quartz radiator bars were swept through the deflected beam in crystal-assisted collimation mode.

The plot of the number of measured protons by the CpFM (for a given position of the bent crystal) is shown in figure 41 as a function of the bar position. The charge of the CpFM signal was measured at a frequency of 43 Hz (1 bunch over 1000), each measurement during 20 s. The signal stays constant till the position 74.5 mm when the bar starts intercepting the deflected beam. At

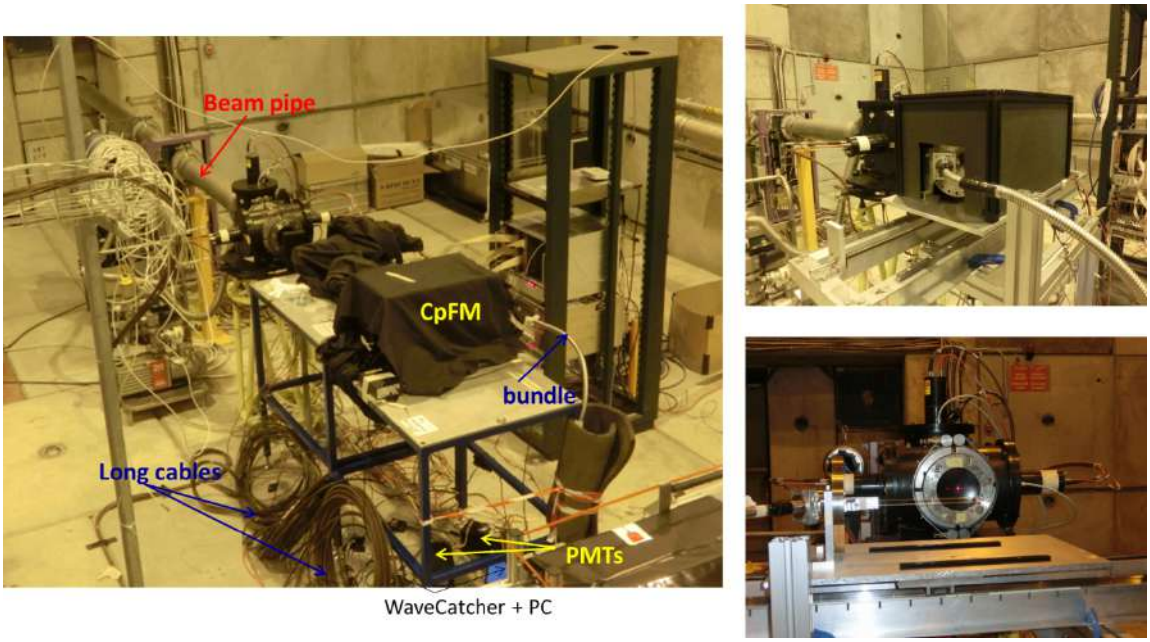

Figure 36. Left: the setup for the tests of the CpFM in H8 — Right top: the CpFM and trigger counters test were enclosed in a box covered with black tissue — Right bottom: alignment of the Quartz bars with the beam.

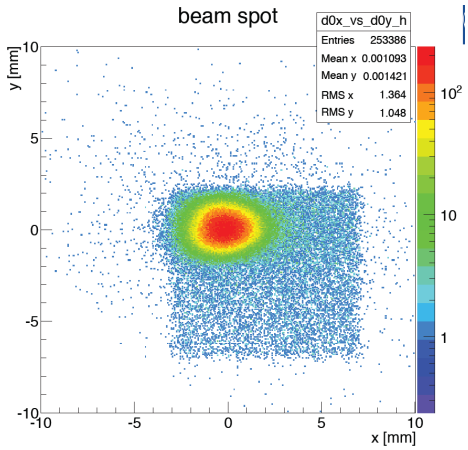

Figure 37. Profile of the proton beam used for the calibration of the CpFM.

79 mm, it intercepts the whole channelled beam and the signal is at its maximum (which corresponds to 12 protons in the bent crystal configuration used for this test). These results are in agreement with the size of this beam evaluated at 4 mm by the Medipix detector [29].

The plot is well interpolated by an Error-function whose derivative is a Gaussian with a sigma of 1.18 ± 0.06 mm. Since the CpFM sits 58.48 m downstream the crystal we can derive an angular spread of the channelled beam of 12 ± 2 μrad in good agreement with the critical angle at 270 GeV [7].

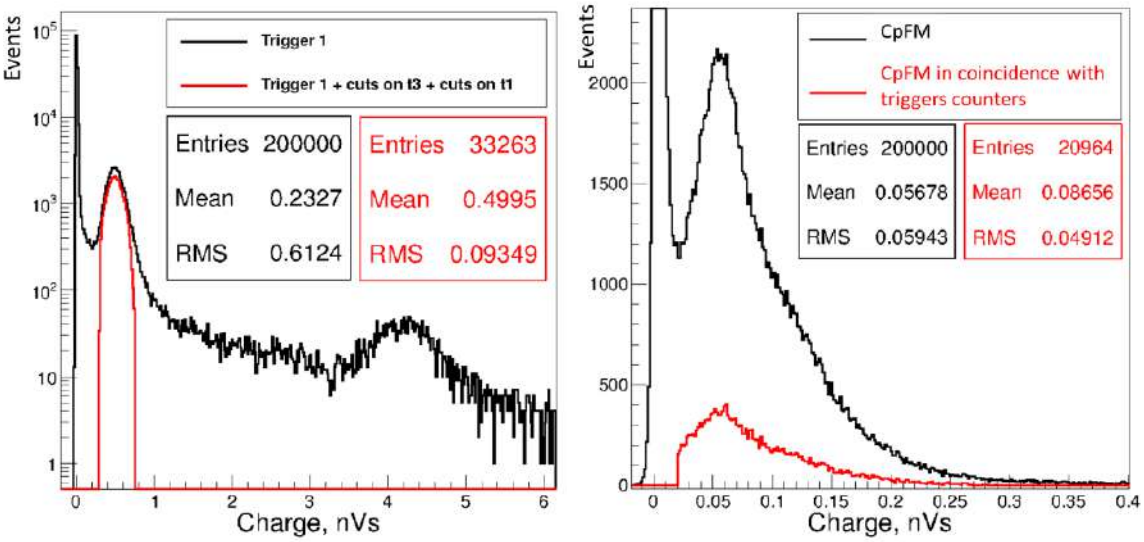

Figure 38. Left: charge distribution of the counter (trigger 1) placed in front of the Quartz bar end (where the protons cross the radiator) — Right: charge distribution of the CpFM. The black histograms correspond to all the events recorded, the red histograms are the result of the different cuts (coincidence with the counters placed upstream and downstream of the Quartz bar).

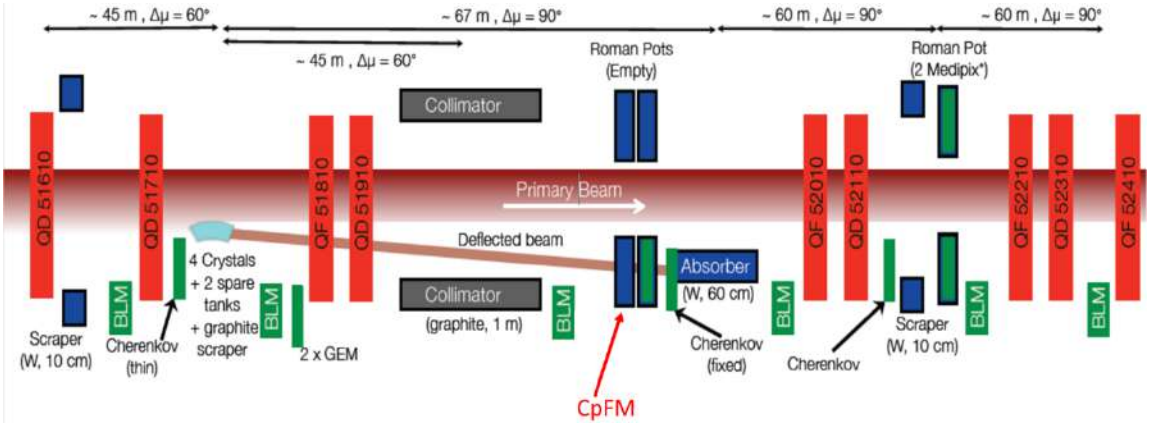

Figure 39. Layout of the UA9 experiment at SPS.

7 Summary

We developed for UA9 the CpFM, a new detector concept based on Fused Silica radiators that monitors the absolute proton flux of the deflected beam and successfully installed a first version of it in the SPS.

Channelled protons produce Cherenkov light in the in-vacuum radiator which is routed to the PMT one meter from the beam pipe by Fused Silica optical fibers to avoid PMT being swamped by radiation background from the accelerator. A dedicated electronics is used to record the signal and allows using the CpFM in coincidence with other devices in the UA9 experiment. The design of this device took into account the requirements for CERN accelerators, fully satisfying the ones for SPS and allowing to identify critical issues for the compatibility with LHC.

2017 JINST 12 P04029

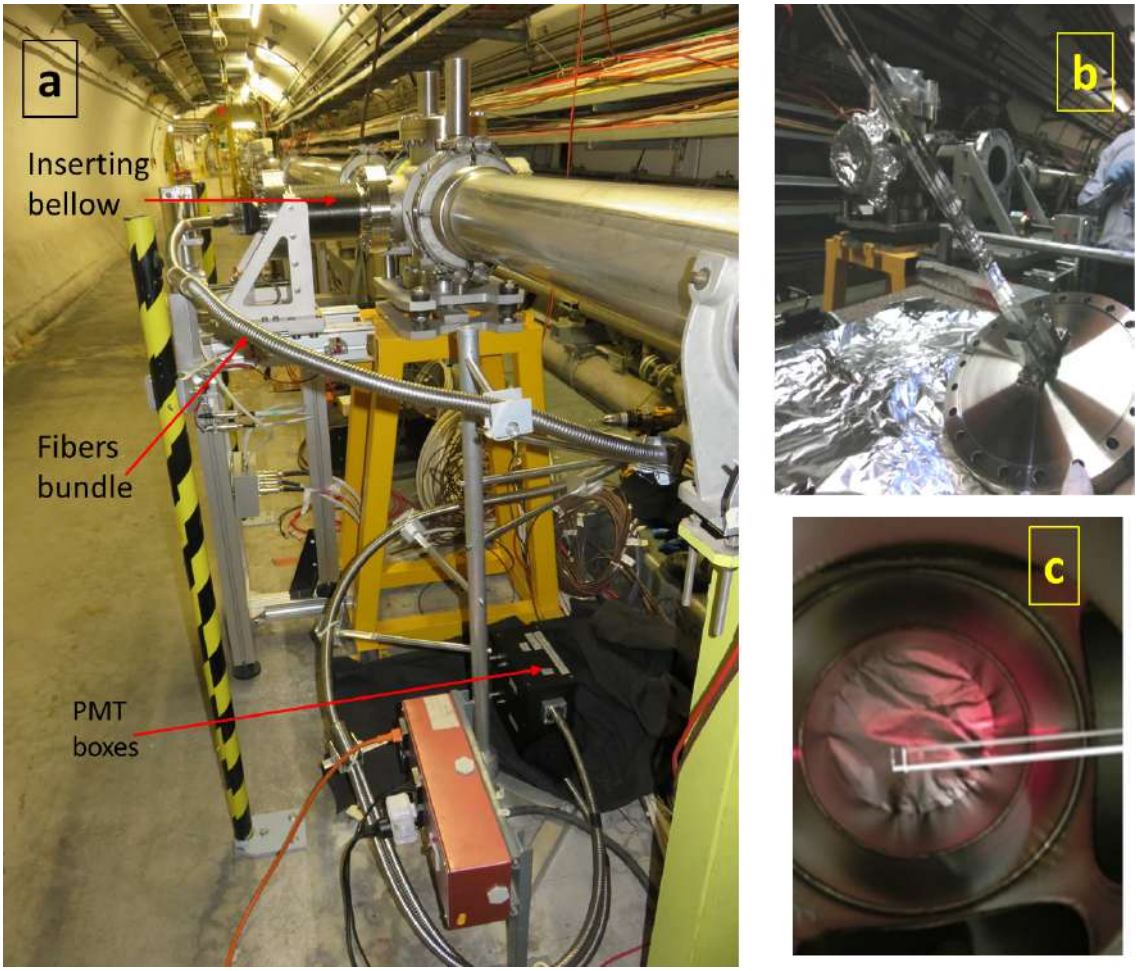

Figure 40. a) The CpFM installed in the SPS ring — b) the 2 Quartz bars attached to the flange — c) laser alignment of the Quartz bars with the center of the beam pipe.

The CpFM, sensitive to single particle, measured the population of deflected beam halo with a resolution of 15%.

The improvement of the CpFM resolution can be achieved by increasing the light yield of the system. Future development aims to build an improved detection chain with a resolution of 5% owing to an optimized geometry and mechanical integration of the radiators (brazing to the flange) as well as an enhancement of the light guide that transports the light to the PMT.

Acknowledgments

We wish to acknowledge the strong support of the BTF team, the CERN EN-STI, BE-RF, BE-OP, EN-MEF and TE-VSC groups.

The INFN authors acknowledge the support of the ERC Ideas Consolidator Grant No. 615089 “CRYSBEAM”.

2017 JINST 12 P04029

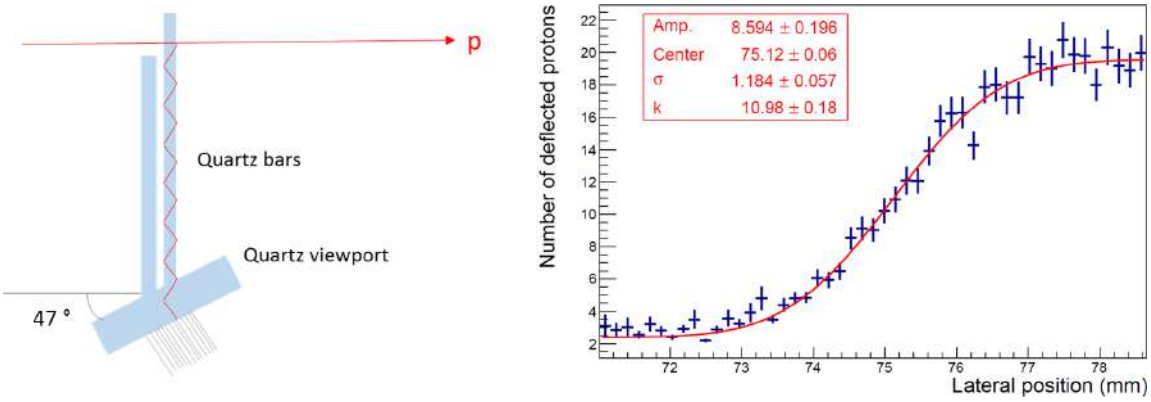

Figure 41. Left: drawing of the CpFM inserted in the proton deflected beam of SPS — Left: number of deflected protons detected by the CpFM as a function of the radiator bar position in the vacuum pipe during crystal assisted collimation of the SPS beam halo of 270 GeV/c protons. The interpolating curve is an Err-function.

References

[1] W. Scandale, *Crystal-based collimation in modern hadron colliders*, *Int. J. Mod. Phys.* **A 25** (2010) 70.

[2] W. Scandale et al., *Observation of strong leakage reduction in crystal assisted collimation of the SPS beam*, *Phys. Lett.* **B 748** (2015) 451 [*Erratum ibid.* **B 750** (2015) 666].

[3] W. Scandale et al., *Observation of channeling for* 6500 *GeV/c protons in the crystal assisted collimation setup for LHC*, *Phys. Lett.* **B 758** (2016) 129.

[4] W. Scandale, *Experimental insertions for the LHC*, in proceedings of the *ECFA Large Hadron Collider (LHC) Workshop: Physics and Instrumentation*, Aachen, Germany, 4–9 October 1990, volume 3, G. Jarlskog and D. Rein eds., CERN, Geneva Switzerland (1990), pp. 760–764 [CERN-1990-010-V-3].

[5] R. Assmann et al., *Requirements for the LHC collimation system*, in proceedings of the *8th European Particle Accelerator Conference (EPAC 2002)*, Paris, France, 3–7 June 2002 [LHC-PROJECT-REPORT-599].

[6] C. Bracco, *Commissioning Scenarios and Tests for the LHC Collimation System*, Ph.D. Thesis, École Polytechnique Fédérale de Lausanne, Lausanne Switzerland (2009) [doi:10.5075/epfl-thesis-4271].

[7] W. Scandale et al., *First results on the SPS beam collimation with bent crystals*, *Phys. Lett.* **B 692** (2010) 78.

[8] M. Gasior, R. Jones, T. Lefevre, H. Schmickler and K. Wittenburg, *Introduction to Beam Instrumentation and Diagnostics*, in proceedings of the *CERN Accelerator School: Advanced Accelerator Physics Course (CAS 2013)*, Trondheim, Norway, 18–29 Aug 2013 [arXiv:1601.04907].

[9] E.B. Holzer, *Instrumentation for space charge effects*, in proceedings of *Space Charge 2013*, CERN, Geneva, Switzerland, 16–19 April 2013 http://cds.cern.ch/record/1542829.

[10] F. Gallucio, private communication.

[11] M. Taborelli, *Codification of surface cleanliness levels*, SOP-AS-01 (2013).

2017 JINST 12 P04029

[12] J. Freeman, *Silicon Photomultipliers for the CMS Hadron Calorimeter*, *Nucl. Instrum. Meth.* **A 617** (2010) 393.

[13] Y. Musienko, A. Heering, M. Wayne, R. Ruchti, A. Karneyeu and V. Postoev, *Studies of Silicon Photomultipliers for the CMS HCAL Upgrade*, PoS(PhotoDet2015)038.

[14] J. Cohen-Tanugi, M. Convery, B. Ratcliff, X. Sarazin, J. Schwiening and J. Va'vra, *Optical properties of the DIRC fused silica Cherenkov radiator*, *Nucl. Instrum. Meth.* **A 515** (2003) 680 [hep-ex/0305001].

[15] M. Hoek et al., *Radiation hardness study on fused silica*, *Nucl. Instrum. Meth.* **A 595** (2008) 190.

[16] S.G. Manufacturers, *Tie-29: Refractive index and dispersion*, (2007) http://www.schott.com/advanced_optics/german/download/schott_tie-29_refractive_index_and_dispersion_eng.pdf.

[17] I. Dumanoglu et al., *Radiation-hardness studies of high OH^- content quartz fibres irradiated with* 500 *MeV electrons*, *Nucl. Instrum. Meth.* **A 490** (2002) 444.

[18] K. Cankoçak et al., *Radiation-hardness measurements of high OH^- content quartz fibres irradiated with* 24 *GeV protons up to* 1.25 *Grad*, *Nucl. Instrum. Meth.* **A 585** (2008) 20.

[19] U. Akgun et al., *Quartz plate calorimeter as SLHC upgrade to CMS hadronic EndCap calorimeters*, *J. Phys. Conf. Ser.* **160** (2009) 012015.

[20] www.leoni-fiber-optics.com.

[21] M. Villa, *The Luminosity Monitor of the ATLAS Experiment*, in proceedings of the *2009 IEEE Nuclear Science Symposium Conference Record (NSS/MIC)*, Orlando, FL, U.S.A., 24 October–1 November 2009 [doi:10.1109/NSSMIC.2009.5402438].

[22] Hamamatsu Photonics K.K., *Photomultiplier Tubes. Basics and Applications*, (2007) http://hamamatsu.com/resources/pdf/etd/PMT_handbook_v3aE.pdf.

[23] D. Breton, E. Delagnes, J. Maalmi and P. Rusquart, *The WaveCatcher family of SCA-based* 12*-bit* 3.2*-GS/s fast digitizers*, in proceedings of the *2014 19th IEEE-NPSS Real Time Conference*, Nara, Japan, 26–30 May 2014 [doi:10.1109/RTC.2014.7097545].

[24] E. Delagnes, Y. Degerli, P. Goret, P. Nayman, F. Toussenel and P. Vincent, *SAM: A new GHz sampling ASIC for the HESS-II front-end electronics*, *Nucl. Instrum. Meth.* **A 567** (2006) 21.

[25] GEANT4 collaboration, S. Agostinelli et al., *GEANT4: A simulation toolkit*, *Nucl. Instrum. Meth.* **A 506** (2003) 250.

[26] L. Burmistrov et al., *Cherenkov detector for proton Flux Measurement for UA9 project*, in proceedings of the *2013 IEEE Nuclear Science Symposium and Medical Imaging Conference (NSS/MIC)*, Seoul, Republic of Korea, 27 October–2 November 2013 [doi:10.1109/NSSMIC.2013.6829430].

[27] A. Danisi et al., *Study and Comparison of Mode Damping Strategies for the UA9 Cherenkov Detector Tank*, in proceedings of the *6th International Particle Accelerator Conference (IPAC 2015)*, Richmond, Virginia, U.S.A., 3–8 May 2015 [CERN-ACC-2015-345] http://cds.cern.ch/search?f=author&p=Danisi%2C%20Alessandro&ln=it.

[28] L. Burmistrov et al., *Test of full size Cherenkov detector for proton Flux Measurements*, *Nucl. Instrum. Meth.* **A 787** (2015) 173.

[29] http://medipix.web.cern.ch/medipix/.

2017 JINST 12 P04029